

Seismotectonics and rupture process of the M_W 7.1 2011 Van reverse-faulting earthquake, eastern Turkey, and implications for hazard in regions of distributed shortening

D. Mackenzie,¹ J.R. Elliott,¹ E. Altunel,² R.T. Walker,¹ Y.C. Kurban,²
 J.-L. Schwenninger³ and B. Parsons¹

¹*Department of Earth Sciences, University of Oxford, Oxford, United Kingdom. E-mail: david.mackenzie@earth.ox.ac.uk*

²*Department of Geological Engineering, Eskisehir Osmangazi University, Eskisehir, Turkey*

³*Department of Archaeology, University of Oxford, Oxford, United Kingdom*

Accepted 2016 April 18. Received 2016 March 23; in original form 2016 January 12

SUMMARY

The 2011 October 23 M_W 7.1 Van earthquake in eastern Turkey caused ~600 deaths and caused widespread damage and economic loss. The seismogenic rupture was restricted to 10–25 km in depth, but aseismic surface creep, coincident with outcrop fault exposures, was observed in the hours to months after the earthquake. We combine observations from radar interferometry, seismology, geomorphology and Quaternary dating to investigate the geological slip rate and seismotectonic context of the Van earthquake, and assess the implications for continuing seismic hazard in the region. Transient post-seismic slip on the upper Van fault started immediately following the earthquake, and decayed over a period of weeks; it may not fully account for our long-term surface slip-rate estimate of ≥ 0.5 mm yr⁻¹. Post-seismic slip on the Bostaniçi splay fault initiated several days to weeks after the main shock, and we infer that it may have followed the M_W 5.9 aftershock on the 9th November. The Van earthquake shows that updip segmentation can be important in arresting seismic ruptures on dip-slip faults. Two large, shallow aftershocks show that the upper 10 km of crust can sustain significant earthquakes, and significant slip is observed to have reached the surface in the late Quaternary, so there may be a continuing seismic hazard from the upper Van fault and the associated splay. The wavelength of folding in the hanging wall of the Van fault is dominated by the structure in the upper 10 km of the crust, masking the effect of deeper seismogenic structures. Thus, models of subsurface faulting based solely on surface folding and faulting in regions of reverse faulting may underestimate the full depth extent of seismogenic structures in the region. In measuring the cumulative post-seismic offsets to anthropogenic structures, we show that Structure-from-Motion can be rapidly deployed to create snapshots of post-seismic displacement. We also demonstrate the utility of declassified Corona mission imagery (1960s–1970s) for geomorphic mapping in areas where recent urbanization has concealed the geomorphic markers.

Key words: Seismic cycle; Geomorphology; Continental tectonics: compressional; Folds and folding; Crustal structure.

1 INTRODUCTION

On 2011 October 23, the cities of Van and Erciş in eastern Turkey were severely damaged by an $M_W = 7.1$ earthquake (Fig. 1), resulting in the death of 604 people. A further 40 died as the result of an M_W 5.7 aftershock on 2011 November 9, which caused further building damage, primarily in the city of Van (e.g. Erdik *et al.* 2012; Elliott *et al.* 2013; Fielding *et al.* 2013). The earthquake, which occurred on a relatively short (~25 km) reverse fault (Fig. 2)

and generated no primary surface ruptures, was one of the largest continental reverse faulting events in recent decades (Wright *et al.* 2013).

The slip solution determined by InSAR for the Van earthquake suggests the fault only ruptured below a depth of ~10 km. As such, there is the potential for another, possibly even more damaging, shallow earthquake if the upper portion of the fault fails seismically (Elliott *et al.* 2013). Alternatively, the upper sections of the fault may creep aseismically; it is known that at least small amounts of

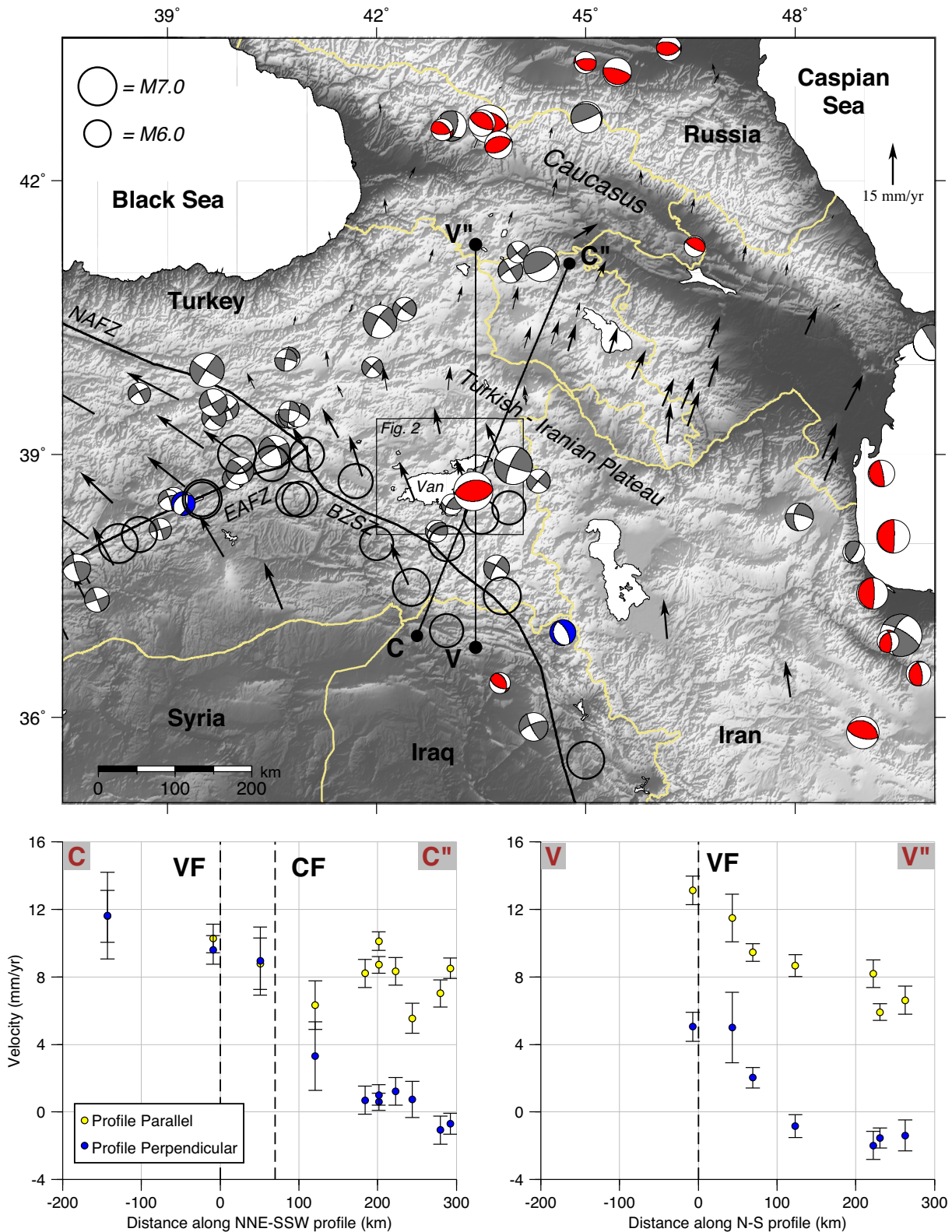


Figure 1. Top: tectonic overview of the Turkish–Iranian plateau, the highlands between Iran and Turkey, where we see the transition from the localized deformation on the north and east Anatolian faults (NAFZ, EAFZ) to distributed shortening and shear accommodated by conjugate strike-slip and thrust faulting. BZSZ marks the Bitlis-Zagros Suture zone between Arabia and Eurasia. Modern earthquake focal mechanisms shown for magnitude > 5 from the Global Centroid Moment Tensor catalogue (Dziewonski *et al.* 1981; Ekström *et al.* 2012). Thrust mechanisms are shown in red, normal in blue and strike-slip in grey. Regional GPS velocity vectors overlaid from Vernant *et al.* (2004), McClusky *et al.* (2000) and Reilinger *et al.* (2006). The box shows the outline of Fig. 2. Bottom: the GPS velocity vectors projected onto the two profiles V–V'' (000°) and C–C'' (022°) demonstrate the distributed nature of shortening and shear across the plateau. The dashed line at zero represents the Van fault (VF). The second dashed line on C–C'' represents the right-lateral strike-slip fault, the Çaldıran fault (CF).

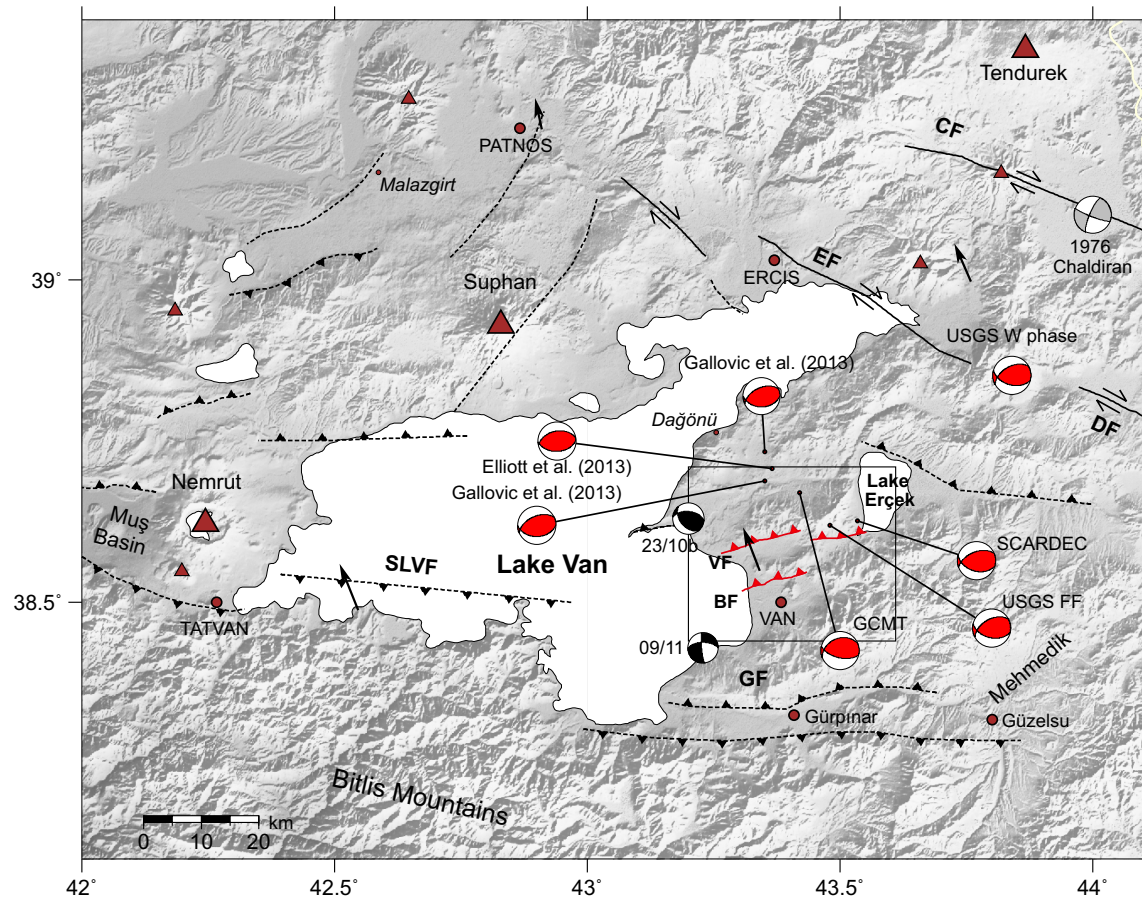


Figure 2. Active fault map of the Van region, based on work by Altinli (1966), Saroglu *et al.* (1992), Karakhanian *et al.* (2004), Ozkaymak *et al.* (2011), Üner *et al.* (2015) and our own field and remote sensing mapping. Solid lines represent faults for which we have strong evidence of activity from earthquakes and/or displaced Late Quaternary markers. Faults marked in red are those shown to have undergone post-seismic motion following the main shock. Dashed lines represent faults inferred from the broader geomorphic markers, but lacking direct evidence for Holocene activity. The black box marks the region shown in Figs 3 and 7. The focal mechanisms in red represent the various fault plain solutions for the 2011 October 23 main shock. The mechanisms in black are for the two large aftershocks—the 23/10/11 mechanism is from bodywave modelling by Elliott *et al.* (2013), while that of the 09/11/11 aftershock is from the USGS solution. Both locations are from the USGS. Triangles denote Holocene volcanic centres. GPS velocity vectors are from Reilinger *et al.* (2006). Fault labels: CF, Çaldıran Fault; EF, Erciş Fault; DF, Dorutay Fault; VF, Van fault; SLVF, South Lake Van fault; BF, Bostaniçi fault; GF, Gürpınar Fault.

post-seismic creep occurred, as was imaged following the main shock (Doğan & Karakaş 2013; Elliott *et al.* 2013). However, the largest aftershock (M_w 5.9) 10 hr after the main shock was associated with shallow slip between 3–10 km depth at the eastern end of the main fault rupture, indicating that this shallower portion of the fault has the potential to be seismogenic (Elliott *et al.* 2013). Therefore, resolving the depth extent of fault frictional behaviour is important for assessing the potential size of a future earthquake and consequent degree of hazard.

In addition to the depth-dependent frictional behaviour, there is the potential for both structural and lithological controls on the depth extent of faulting. Lithological layers such as salt and shale detachment horizons act to compartmentalize slip in narrow depth extents (Nissen *et al.* 2010; Elliott *et al.* 2015a), and the intersection of faults at depth has been suggested as a possible (albeit potentially temporary) barrier to rupture propagation (Elliott *et al.* 2011, 2016). There has been much discussion on the effect of along-strike segmentation on the length of ruptures in strike-slip earthquakes (e.g. Wesnousky 2008), but much less for downdip segmentation in dip-slip earthquakes in intracontinental settings. The rapid

post-seismic motion observed with InSAR following the Van earthquake images the faulting in the upper 10 km of the crust, allowing us to probe the influence of structure on slip propagation.

Further south from the Van fault (VF), Doğan *et al.* (2014) noted motion on a splay fault (the Bostaniçi fault, BF, Fig. 2) at the surface within the northern limits of the city of Van using post-seismic GPS and InSAR data. We add further remote sensing observations and field evidence of the surface expression of this splay fault. In addition, we demonstrate the utility of two novel data sets in assessing and monitoring Quaternary and modern geomorphology within expanding cities—the exploitation of 1960s–1970s declassified US spy satellite imagery (Hollingsworth *et al.* 2012); and the rapid, very low cost, photogrammetric mapping using Structure from Motion (SfM; James & Robson 2012; Johnson *et al.* 2014).

Combining the tectonic geomorphology across the region with Quaternary dating, we determine the long term slip-rate on the VF. Studying the immediate post-seismic behaviour and the longer-term slip rate allows us to probe the earthquake cycle in this region of the Arabia-Eurasia collision zone where the cycle is much longer than the instrumental catalogues and often the historical records too.

2 BACKGROUND TO THE VAN EARTHQUAKE

2.1 Tectonic setting

The Van region lies in a zone of general north–south shortening within the continental collision zone between Arabia and Eurasia (e.g. Copley & Jackson 2006). Early estimates suggest that the initial collision was at ~ 10 Ma (Dewey *et al.* 1986), though palaeoclimate studies suggest it may have begun as early as ~ 35 Ma (Allen & Armstrong 2008). Much of the current rate of Arabia–Eurasia convergence (23 mm yr^{-1}) is accommodated by shortening in the Caucasus, but around $\sim 10 \text{ mm yr}^{-1}$ is distributed across the Turkish–Iranian Plateau (TIP; Reilinger *et al.* 2006). In western Turkey, Arabia–Eurasia shortening results in the westwards extrusion of Anatolia in a plate-like fashion, bounded by the north Anatolian and east Anatolian faults (e.g. McClusky *et al.* 2000; Reilinger *et al.* 2006), whereas eastern Turkey is a zone of distributed crustal shortening (Fig. 1).

Shortening within the TIP is accommodated by a combination of thrust and conjugate strike-slip faults (Figs 1 and 2). The 2011 Van earthquake occurred on a thrust fault approximately 10 km north of Van which was previously unrecognized as active (Doğan & Karakaş 2013; Elliott *et al.* 2013; Fielding *et al.* 2013). There have been a number of large historical earthquakes in the Van region, the most recent of which was the 1976 $M_W = 7.1$ Çaldıran strike-slip earthquake ~ 80 km northeast of Van (Fig. 2), which caused heavy damage in the town of Çaldıran and much of the surrounding region (Gülkan *et al.* 1978).

Monastery archives record several damaging historical earthquakes in the region, including the 1648 Van-Hayotsdzor earthquake, estimated to be $M \sim 6.7$, which caused heavy damage in the region from Van south to the Gürpınar valley (Fig. 2), completely destroying or damaging beyond repair at least 11 different monasteries across the region (Ambraseys 1989). In 1715, an $M 6.6+$ earthquake occurred southeast of Van in the region of Mahmatan, causing damage in the Mehmedik plain (Fig. 2), ruining the walls of the Hoşap Castle (modern town of Güzelsu, ~ 40 km southeast of Van), but potentially causing damage as far as Erciş (Thierry 1979; Ambraseys & Melville 1982; Ambraseys 1989). In 1903, the $M_S 7.0$ Malazgirt earthquake to the northwest of Lake Van, was reported to have killed at least 700 people (Shebalin *et al.* 1997). Utkucu (2013) suggest that the 1715 event may have occurred on the same fault as the 2011 event, but it is difficult to associate these historical earthquakes with specific faults with much certainty, as there are no records of surface ruptures.

2.2 Geological setting

Van lies on the eastern shore of the alkaline Lake Van, which has a mean elevation of 1650 m above mean sea level (Kadioğlu *et al.* 1997). To the north and west of Lake Van, the exposed geology is predominantly composed of Quaternary and Neogene volcanics (Pearce *et al.* 1990). To the south of Lake Van, the Bitlis mountains rise to ~ 3500 m, and are comprised of Palaeozoic and Mesozoic metamorphic and ophiolitic lithologies. Around the city of Van, are regions of Pliocene basin deposits, Quaternary lake sediment deposits and extensive Quaternary volcanics (MTA 2002; Kuzucuoğlu *et al.* 2010), most of which have been faulted, folded and tilted by tectonic activity.

The presence of soft sediment deformation structures (seismites) in the varved lake sediments provides a rich record of prehistoric

earthquakes in the Van region. Üner *et al.* (2012) map several different varieties of seismites at six different locations around the south and east shores of Lake Van, which they attribute to occurrence of repeated $M_W > 5$ earthquakes in the Late Quaternary. The recent International Continental Drilling Project (ICDP) PALAEO-VAN project has focused on coring the varved sediments from two locations within Lake Van (Litt *et al.* 2009, 2012; Cukur *et al.* 2014; Litt & Anselmetti 2014; Stockhecke *et al.* 2014). Work is ongoing to establish the chronology, but Litt *et al.* (2009) observe extensive seismites in the test drill cores, attributing them to the repeated occurrence of earthquakes throughout the last 500 ka.

2.3 The 2011 October 23 Van earthquake

Initial epicentres for the 2011 main shock were as far apart as ~ 20 km, but later solutions incorporating radar interferometry tie the location to ~ 22 km due north of Van (Fig. 2). A summary of the seismological and geodetic solutions is shown in Table 1.

InSAR, seismology, GPS and combined solutions (Zahradnik & Sokos 2011; Irmak *et al.* 2012; Doğan & Karakaş 2013; Elliott *et al.* 2013; Fielding *et al.* 2013; Gallovic *et al.* 2013; Feng *et al.* 2014; Moro *et al.* 2014; Zahradnik & Sokos 2014; Wang *et al.* 2015), broadly agree that the earthquake occurred on a steep north dipping ($40\text{--}55^\circ$) fault, with a small left lateral component. The upper extent of slip is generally agreed to be 7–10 km depth. Chequerboard tests by Elliott *et al.* (2013) show that this top depth is well constrained by the InSAR data. The pattern of uplift is consistent with the field observations of Emre *et al.* (2011), who observed uplift of the lake shore (inferred from the height of shoreline boulder deposits) of up to ~ 40 cm near the village of Dağönü. The source models of Elliott *et al.* (2013), Zahradnik & Sokos (2014) and Wang *et al.* (2015) go further in breaking the rupture into two smaller discrete patches of slip or sub-events, possibly on two fault segments aligned to two geomorphic scarps.

The majority of well constrained aftershocks were shallow, in the 0–10 km region, and appear to cluster around the uppermost edge of the rupture region (Fielding *et al.* 2013), but the cumulative moment release from the aftershocks over the entire region is still small compared to that of the main shock (< 10 per cent over the first 3-months, based on the ISC bulletin). Two large aftershocks occurred in the hours to days following the earthquake. A $M_W 5.9$ aftershock occurred towards the northeastern extent of the fault 10 hr after the main shock with a thrust mechanism similar to the main shock (Irmak *et al.* 2012; Elliott *et al.* 2013). The $M_W 5.7$ aftershock on 9th November 2015 had a strike-slip/oblique mechanism and was located to the southwest of the VF, within Lake Van (Fielding *et al.* 2013).

3 METHODS—STRUCTURE FROM MOTION SURVEYING

One of the fundamental measurements in characterizing active faulting from geomorphic markers is determining fault offsets in topography, due to motion in single or multiple events. In the simplest case of a uniform fault scarp running through a flat surface, a basic differential GPS (DGPS) profile can be used to measure of the offset in the surface. However, as the surface becomes more uneven, or the strike of the fault changes, it becomes necessary to look at the offset over a larger area and terrain range and take an average. Similarly, if we wish to differentiate between individual events (such as multiple lateral offsets of different amounts), it becomes

Table 1. Table of earthquake mechanisms for the Van Earthquake main shock from various authors mentioned in the text. 1f and 2f refer to the single fault and two fault models.

Source	Data set	Lat (°)	Long (°)	Centroid depth (km)	M_W	Moment (10^{19} Nm)	Strike (°)	Dip (°)	Rake (°)	Slip (m)	Top (km)	Bottom (km)
KOERI	Seismic	38.73	43.43	5	6.6(M_L)							
GCMT	Seismic	38.67	43.42	12	7.1	6.40	246	38	60			
USGS	Seismic	38.69	43.49	16	7.1	6.40	255	50	73			
USGS–W	Seismic	38.69	43.49	16	7.1	5.60	241	51	58			
GFZ	Seismic	38.72	43.55	10	7.0	4.70	268	36	85			
EMSC	Seismic	38.86	43.48	10	7.2	6.80	248	53	64			
Elliott <i>et al.</i> (2013)	Seismic	38.67 ^a	43.42 ^a	19	7.0	3.26	243	50	60			
Irmak <i>et al.</i> (2012)	Seismic	38.782	43.337	15	7.1		246	46	59	3.6	11	24
Fielding <i>et al.</i> (2013)	Seismic	38.69 ^b	43.49 ^b	18	7.1	5.37	258	46	71	3.5	6	29
Utkucu (2013)	Seismic	38.69 ^b	43.49 ^b	11	7.1	4.60	255	50	73	5.5	5	20
Gallovic <i>et al.</i> (2013) ^c	Seismic	38.689	43.351	10	7.2	7.40	246	52	75			
Feng <i>et al.</i> (2014)	SAR	43.403	38.702	12	7.03		261	49	80	6.5	8	
Elliott <i>et al.</i> (2013)-1f	SAR	38.592	43.386	14.1	7.0	4.44	258	45	83	3.7	8.6	19.6
Elliott <i>et al.</i> (2013)-2f	SAR			13.7/13.8	6.8/6.8	2.13/2.31	254	40/55	64/93	3.3/6.7	8.3/10.2	19.1/17.4
Fielding <i>et al.</i> (2013)	SAR				7.1	5.84	259	42.5			6	30
Wang <i>et al.</i> (2015)-2f	SAR			25/25	7.19	6.08	253/253	40/54				

^aFixed to the Global CMT (GCMT) location.

^bFixed to the USGS location.

^cSolution used as the assumed fault plane by Zahradnik & Sokos (2014) who estimate a total moment release of $3.55\text{--}3.87 \times 10^{19}$ Nm in two subevents.

necessary to take a full 3-D view of the fault expression at the surface. For small areas, this can still be done with kinematic DGPS, simply by walking the antenna over the ground (e.g. Campbell *et al.* 2015). But for larger areas, this procedure becomes too time consuming to achieve sufficient resolution. Instead we implement a work flow using photogrammetric reconstruction by SfM, based on the methods of James & Robson (2012), Fonstad *et al.* (2013) and Johnson *et al.* (2014). This is a highly scalable technique, the utility of which we demonstrate from scales of small (<10 cm) creep offsets to much larger (5+ m) fault scarp offsets.

SfM uses many photographs taken from a variety of perspectives, to construct a scale-independent 3-D model. Supplementing this with accurately determined ground control points, we can make digital elevation models (DEMs) with centimetric resolution. Traditional photogrammetry relied on a small number of photos from well calibrated metric cameras, with multiple ground control points necessarily visible in every photograph. In contrast, the SfM method uses the redundancy of many highly overlapping photographs to use a new feature identification algorithm (Scale Invariant Feature Transform, SIFT; Lowe 2004) to simultaneously solve for the relative camera positions and calibration parameters, by matching features between photos. This is followed by a multiview stereo image correlation based reconstruction in a purely relative space, based on the calculated camera orientations. A minimum of three ground control points within the model are required to orient and scale the model.

We use the Agisoft Photoscan commercial software to perform the photogrammetric reconstruction, first using a sparse reconstruction to solve for the internal and external camera parameters, and then a multiview stereo reconstruction to generate a dense pointcloud. The pointcloud is then scaled and oriented using a small number (typically 5–10) of ground control points consisting of orange plastic squares pegged into position and whose location is measured using realtime kinematic (RTK) DGPS. The pointcloud is gridded using a tensioned minimum curvature algorithm, under the Generic Mapping Tools package (GMT; Smith & Wessel 1990), to generate a DEM. The gridded data is appropriate for hillshading and display (Section 5.2.2), but analysis is performed on the raw

dense pointcloud. We manually mask any regions of the pointcloud where the geomorphic marker has been modified, before measuring displacements.

In this study we perform two different types of SfM survey; for small offsets in anthropogenic markers which can easily be viewed from many viewpoints, we use a handheld compact digital camera, while for larger terrain offsets (scarps) we use a camera mounted on a long pole to gain an elevated perspective. The survey design is important in determining the ability of the SIFT algorithm to match features between photos—photos were taken with significant overlap typically >60 per cent and minimal change in orientation (10°). In the case of the pole survey (Section 5.2.2), we used a compact digital camera (Ricoh GR11) mounted on a 6 m aluminium pole. The camera is oriented downwards but angled forwards at $\sim 20^\circ\text{--}30^\circ$, just clear of the operator, in order to incorporate a greater depth of field (DOF) in the photographs (and remove the operator from the frame). A 28 mm (full-frame equivalent) focal length camera provides a field of view of $\sim 11 \times 12$ m on the ground, so we walk a grid at 10 m spacing, covering an area of $\sim 190 \times 150$ m. The pole was carried in a rough grid pattern across the scarp, with adjacent (overlapping) ‘tracks’ moving in opposite directions. A simple downward (nadir) looking geometry would provide the easiest approach, with the best photograph overlap and feature matching, but this results in very limited DOF in the photographs. That parallel-axis geometry with limited DOF results in a trade-off between the focal length and radial distortion coefficients when solving for the lens parameters, resulting in uncorrected image distortion that propagates into the whole model as a ‘bowl’ effect (James & Robson 2014). Our opposing geometry with the angled camera and pre-calibration, avoids the special-case of parallel geometry so we can solve for the lens parameters without ambiguity, even in scenes with relatively poor texture (e.g. grassy fields).

4 POST-SEISMIC SLIP: INSAR AND FIELD MEASUREMENTS

The very rapid first acquisition of post-earthquake COSMO-SkyMed data (4 hr), has provided a valuable opportunity to probe

Table 2. Acquisition dates of the various interferogram pairs discussed in the text. CSK, COSMO-SkyMed; TSX, TerraSAR-X; ASAR, Envisat (the latter in the period after loss of orbit stability). Asc refers to ascending tracks, while dsc refers to descending tracks. The perpendicular baseline is the average between that at the top and bottom of the scene.

Interferogram	Orbit	Date 1 (yyyy-mm-dd)	Date 2 (yyyy-mm-dd)	Perpendicular baseline (m)	Incidence angle (°)	Postseismic period (days)
CSK1	dsc	2011-10-10	2011-10-23	194	28	0–0.167
CSK2	dsc	2011-10-10	2011-10-26	115	28	0–3
CSK3	dsc	2011-10-23	2011-10-26	309	28	0.167–3
TSX1	asc	2011-10-31	2011-11-11	194	33	8–19
TSX2	dsc	2011-11-09	2011-11-20	14	26	17–28
TSX3	dsc	2011-12-01	2012-01-03	29	26	39–72
ASAR1	dsc	2010-11-05	2011-10-31	138	41	0–8
ASAR2	dsc	2011-07-22	2011-11-19	221	41	0–27

the early post-seismic motion. The COSMO-SkyMed interferogram for the coseismic period (CSK1, Table 2) showed minimal surface discontinuities from the earthquake itself. However, interferograms for the period immediately following the earthquake (CSK3, 4 hr to 3 d after) show a small discontinuity at the surface (Doğan & Karakaş 2013; Elliott *et al.* 2013; Feng *et al.* 2014), coincident with surface displacements of up to 10 cm observed in the field (Emre *et al.* 2011). It is likely therefore that most of the observed surface displacements occurred post-seismically, over the two weeks following the main shock (discussed below). In the following sections we further refine measurements of the post-seismic slip, using both field measurements and InSAR. These motions provide important constraints on fault behaviour, as well as providing an insight into the upper crustal structure of the VF and associated splay, and potential controls on rupture propagation.

4.1 Field measurements of post-seismic slip

4.1.1 Van–Erciş Highway

Very shortly after the main shock (1–5 d), a series of small surface ruptures (typically <20 cm) were observed on the main Van–Erciş highway (S1 in Fig. 3). The ruptures are indicative of oblique shortening, including cracking and folding of tarmac, displacement of kerbstones and paved surfaces, and shallow cracking and moletracks across agricultural fields (Emre *et al.* 2011; Ozkaymak *et al.* 2011; Doğan & Karakaş 2013; Elliott *et al.* 2013). The ruptures are along strike from a fault exposure at the Van–Erciş highway, which dips 45–50°N in late Pleistocene deposits (photograph in Fig. 4c). The fringe rate in the coseismic (CSK1) interferogram is too high to distinguish phase discontinuities at the level of 1–2 fringes (<3 cm LOS) so, re-inspecting the coseismic interferogram, we cannot rule out motion during the earthquake. However, we know from the post-seismic interferograms (see below) that significant motion did occur post-seismically.

The road surface has since been repaired, but the kerbstones record the full displacement (Fig. 4a). Using SfM (see Section 3), we created a 3-D terrain model (Fig. 4b) of the road and pavement in order to accurately quantify the displacement at the surface, such that we can compare the observed slip with that imaged in the post-seismic interferograms. The length of six kerbstones measured in the field was used to accurately scale the model. We measure an offset of 23 ± 3 cm laterally and 11.7 ± 1.0 cm vertically (Fig. 4) in the kerblines, as of 24th May 2014. The displacements are consistently observed in each of the four kerblines of the dual-carriageway and are coincident with the exposed fault in the road cutting. They are

also along strike from a topographic scarp of probable Holocene age (Section 5.2).

4.1.2 Splay fault

Post-seismic slip on a southern fault strand, within the northern suburbs of Van city, was imaged using the TSX1 interferogram by Doğan *et al.* (2014) and Wang *et al.* (2015). Reprocessing this interferogram with minimal downsampling (below) enabled us to show that this displacement occurred within a zone no more than ~200 m wide, which we targeted for field investigation. Using the approximate location derived from InSAR we examined optical imagery and topographic data sets. The Shuttle Radar Topography Mission (SRTM) and the Global Digital Elevation Model (GDEM) data sets both show a low south-facing scarp running E-W through the Altintepe and Iskele districts on the northern edge of Van (Fig. 3), roughly paralleling the train tracks and reaching the coast at the port.

We use declassified Corona reconnaissance imagery from one of the Key Hole satellite missions (KH-4B, data available from the U.S. Geological Survey, nadir ground resolution of 1.8 m) to view the region prior to the northward urban expansion of Van. Fig. 5 shows the Corona scene from 20 July 1970, on which we identify the faint trace of a scarp from minor stream incision and shadowing on its uplifted northern side. By comparing the historical imagery to the modern WorldView-2 imagery (0.5 m), we identified several sites for field study where the fault cuts modern roads and buildings. From inspection of high-resolution optical imagery on the Google Earth historical archive, we can see that the majority of the roads in a narrow band along the scarp (coincident with the post-seismic deformation imaged with InSAR) were re-surfaced approximately 1–2 yr after the earthquake. Most of the current road surfaces are therefore not an appropriate record of the total post-seismic deformation. Though the reason for resurfacing is not clear, it is likely that the roads were re-surfaced due to damaged tarmac as a result of post-seismic motion. The only exception is the main road leaving Van to the north, which does not appear to have been resurfaced (2014 May 24), but showed signs of needing repair from cracking in the tarmac (Fig. 6d, location in Fig. 5).

In order to measure the total discrete post-seismic surface slip, we primarily focused our field investigation on the kerblines, walls, and buildings. Examples of deformed kerbstones and walls are shown in Fig. 6. Verbal reports from local residents suggest that the wall in Fig. 6(a), which was built in 1993, was intact immediately after the earthquake, and that the visible extensional cracks have occurred between 2011 and 2014, that is, post-seismically. The cracking in this wall is consistent with uplift on the northern block. In contrast to the surface displacements on the main VF, we find no clear

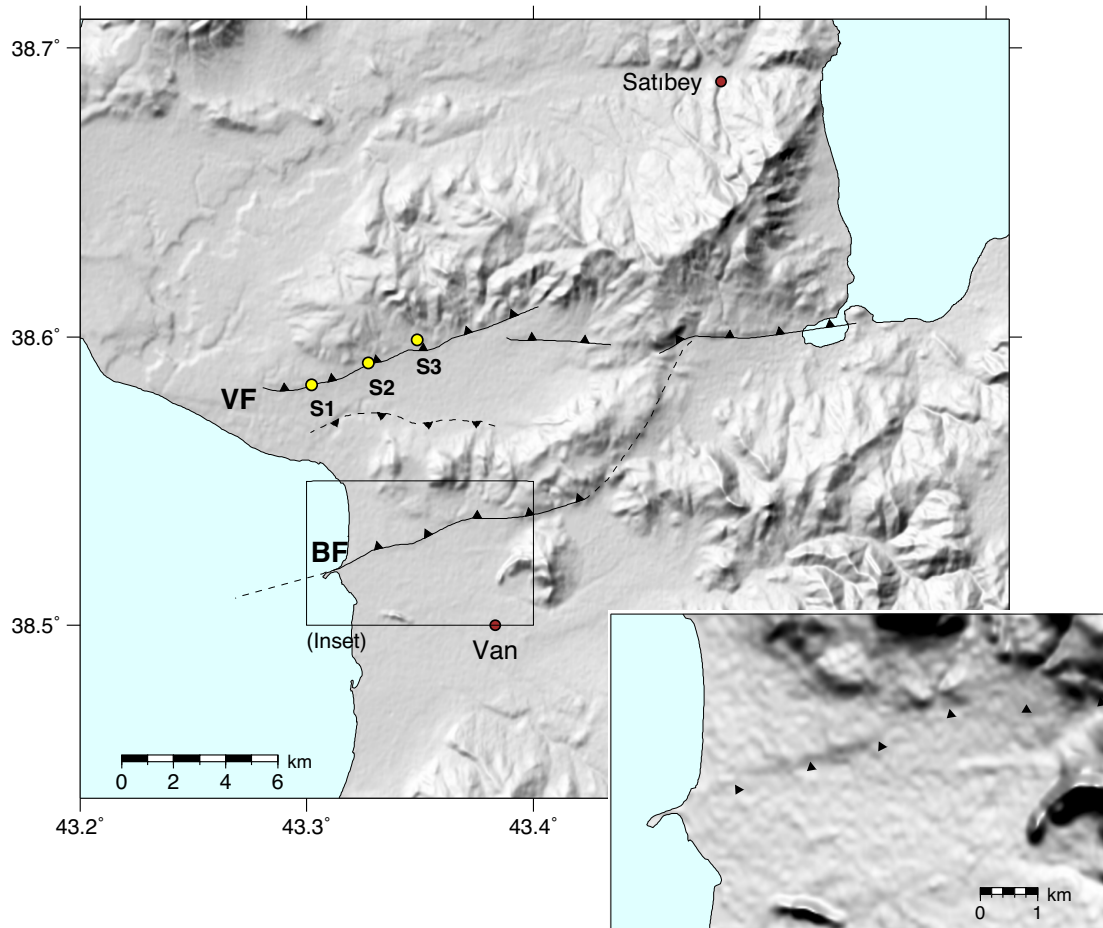


Figure 3. Map of the field study region covering the same region as the interferograms in Fig. 7, on a hillshaded Shuttle Radar Topography Mission (SRTM, 30 m, illuminated from the northwest) basemap with the Van fault (VF) and the Bostaniçi fault (BF) marked and the individual field study sites shown (S1, S2, S3). The backthrust is marked as a dashed line, as is the possible lakeward extension of the BF. We infer from the topography that in the east the fault motion collapses back onto a single strand (connected by a dashed line), consistent with the trace mapped by Doğan *et al.* (2014) and Wang *et al.* (2015). The inset shows the zoom of the northern Van city, with trace of the Bostaniçi splay fault visible in the SRTM elevation data (marked with black triangles). This splay fault is laterally extensive and cuts palaeolake shorelines.

evidence for lateral displacements on this fault. The damaged walls and buildings are superimposed on the pre-existing scarp shown in Fig. 6(f). Using kinematic DGPS, we measured the vertical total offset across the scarp to be $\sim 5.5 \pm 0.5$ m.

The kerbstones of both carriageways of the main road leaving Van to the north showed clear displacements with the north side uplifted where it crosses the splay fault, and the tarmacked surfaces are distorted (see Figs 6c and d). The road does not appear to have been resurfaced post-earthquake and the deformation of the tarmac road surface is coincident with the displacement gradient imaged in the post-earthquake InSAR. Despite not being resurfaced, we suspect that deformation of the tarmac will still have been modified by the impact of vehicles driving over it in the intervening years. However, the kerbstones also appear not to have been replaced since the earthquake, and so are more likely to reliably represent the total post-seismic motion on the splay fault since the earthquake. We constructed a digital surface model of the road section around the kerb offsets, using SfM (see Section 3) with a hand held compact camera. The resulting 3-D model was scaled from tape-measure length measurements of two sets of six kerbstones, agreeing to within 1 per cent. From the scaled surface model we measured 2–4 cm of discrete vertical displacement and negligible lateral displacement.

4.2 Post-seismic InSAR

In order to place firm constraints on the timing, spatial variability and magnitude of post-seismic slip, we re-processed the post-seismic interferograms CSK3, TSX1, TSX2 and TSX3 (first 3 months after the earthquake, described in Table 2). The InSAR data were processed using the ROI_PAC software (Rosen *et al.* 2004), multilooked to four looks in range and azimuth (5 m final pixel size), with branch cut unwrapping. We use minimal down-sampling in order to constrain the location of the splay fault for field study. Further InSAR data from the TerraSAR-X mission was available, with regular acquisitions through to the end of January 2012 (through the Supersites web page <http://supersites.earthobservations.org/van.php>), but these interferograms generally showed very poor coherence—most likely due to winter snow cover, confirmed by inspection of the Landsat ETM+ archive. The four interferograms processed show good coherence near the shores of Lake Van, but poor coherence to the east in the areas of higher topography due to topographic decorrelation and localized snow cover.

Fig. 7 shows the wrapped and unwrapped interferograms, in which we observe significant deformation following the earthquake, localized on two different faults: the VF, and the Bostaniçi splay in the northern suburbs of Van. The faults are identified by high phase

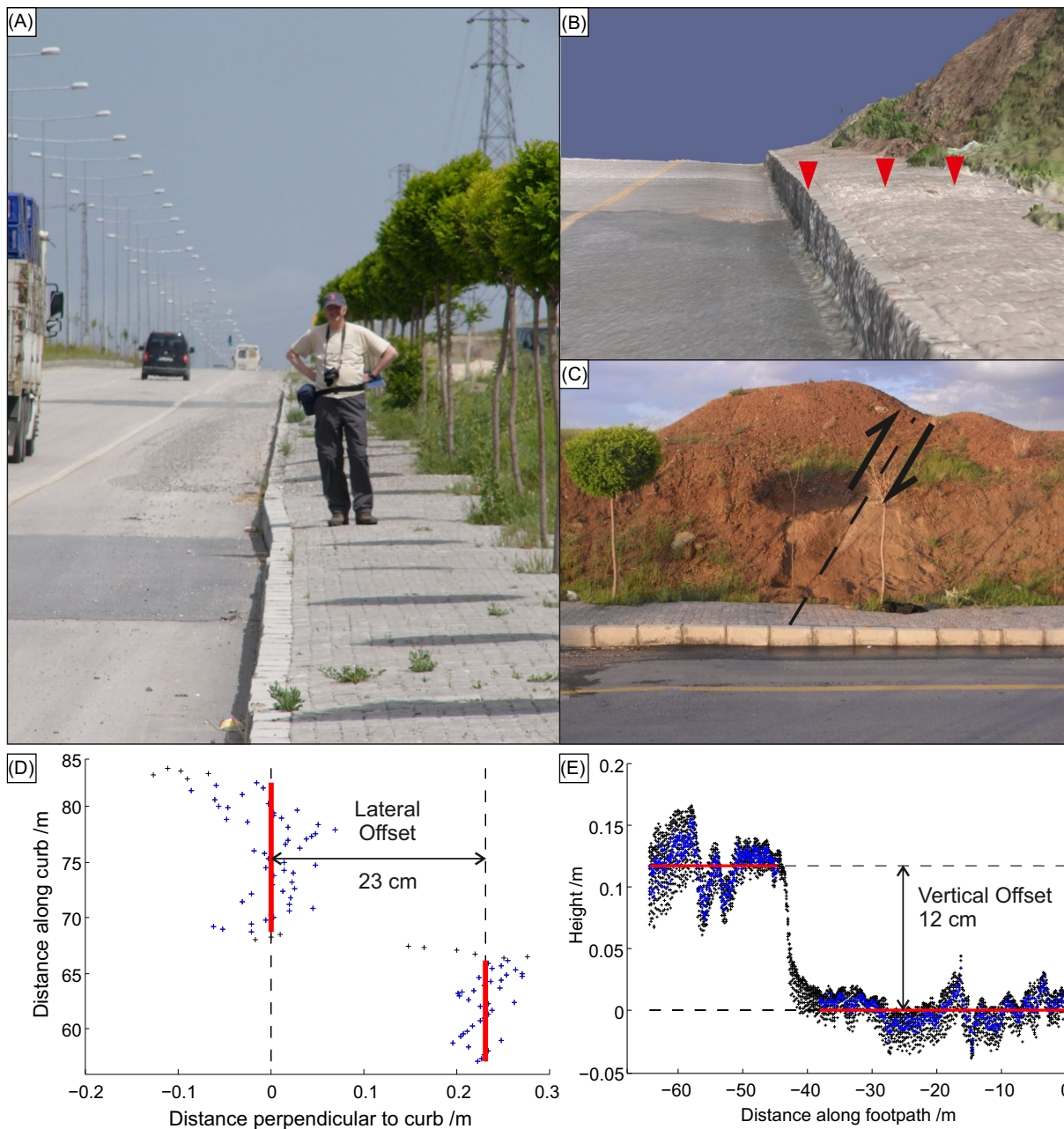


Figure 4. (a) Photograph looking along kerblines (May 2013), person for scale, showing left lateral displacement. (b) Oblique 3-D perspective view of the structure-from-motion reconstruction, showing a vertical offset in the same kerblines. Red arrows denote the displacement line. The poorly correlated trees have been removed from the model ($3\times$ vertical exaggeration to aid visualization). (c) Photograph of the cleaned road cutting, with contrast between hanging-wall and footwall sediments, with coincident displaced kerbstones in the foreground. Dashed line and arrows mark the visible fault dipping 45° N. (d) Horizontal profile along the top edge of the kerblines in the SfM pointcloud showing $\sim 23 \pm 3$ cm lateral offset. Points shown in blue are those used for least squares fit. (e) Vertical profile along the top edge of the kerblines in the SfM pointcloud showing $\sim 11.7 \pm 1.0$ cm vertical offset. A gradient has been removed to de-trend the profile and aid visibility of the vertical offset.

gradients and phase discontinuities that correlate well from scene to scene and map closely to the observed surface displacements. Note that both the large aftershocks mentioned in Section 2.3 are captured by these interferograms. The M_w 5.9 aftershock 10 hr after the main shock is within the CSK3 scene and is likely responsible for the enhanced uplift at the eastern end of the VF (Elliott *et al.* 2013). The second aftershock, M_w 5.7 on 2011 November 9, is captured by both TSX1 (ascending) and TSX2 (descending), and is visible as a series of concentric fringes in the wrapped image of TSX2 (Fig. 7).

To study the spatial and temporal variability of the uplift associated with the fault motion, we take three fault perpendicular profiles (swath width 1.5 km) through the interferograms, A–C (Fig. 8). The CSK3 interferogram (0–3 d) shows a line-of-sight (LOS) displacement signal associated with the VF across all three profiles, with a wavelength of ~ 6 – 7 km, a magnitude of ~ 3 cm and a discontinuity at the mapped fault trace (2–3 cm in LOS). There is little motion on the Bostaniçi splay fault in this interval.

The TSX1 ascending pass interferogram shows a small discontinuity of ~ 1 cm at the VF and a larger step of 2–3 cm at the

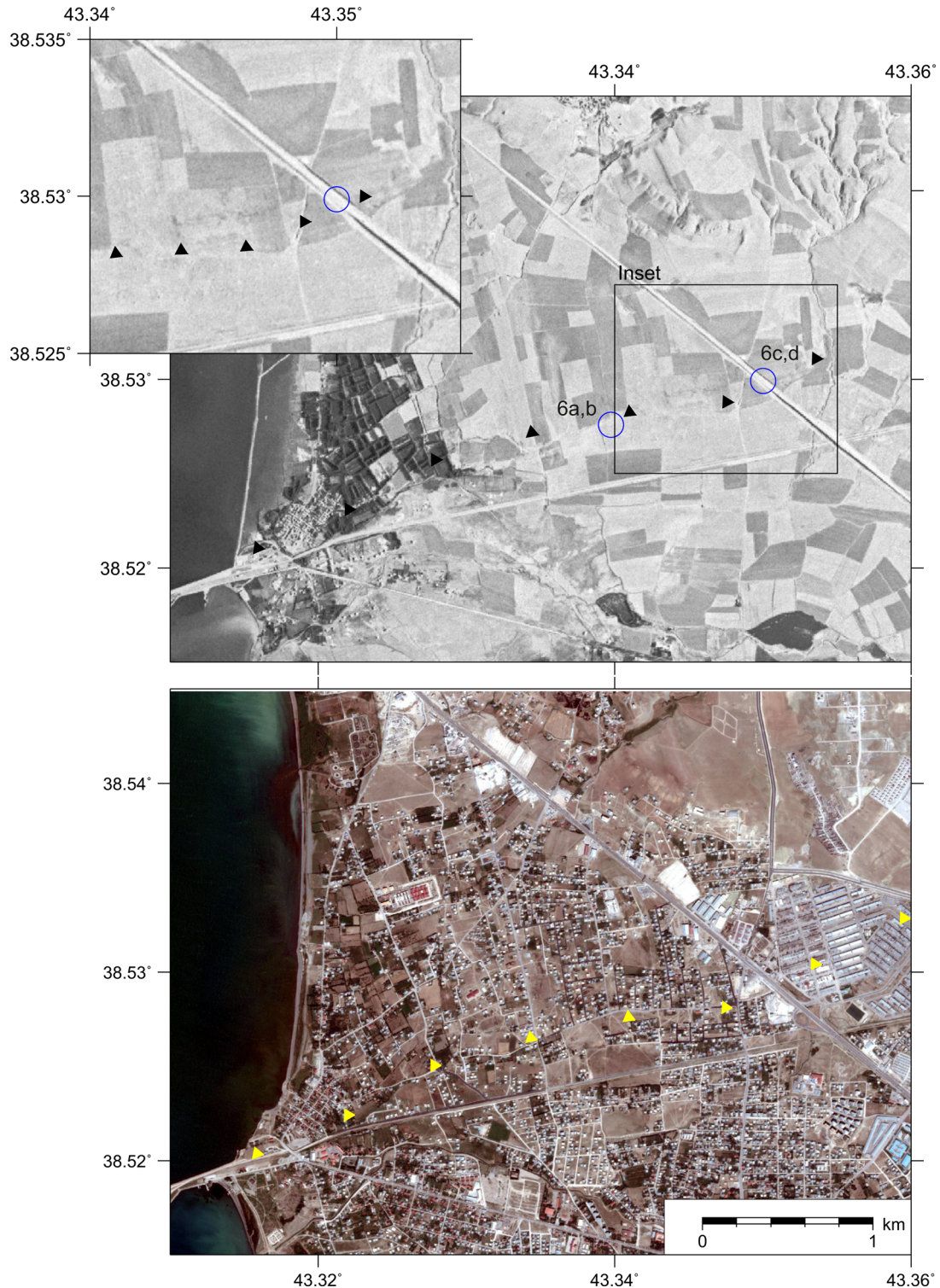


Figure 5. Top: declassified satellite photograph from the Corona mission, 1970 July 20 July, prior to much of the urban sprawl of Van. Circles show the field sites shown in photos in Fig. 6. Black triangles denote the trace of the fault scarp on the Bostaniçi fault. Bottom: modern satellite image (Google Earth, Imagery from CNES/Astrium, Image date:19/07/2013) showing the same region, with much of the morphology covered by urban dwellings. Yellow triangles denote the same trace.

splay fault, with a broad signal of ~ 4 cm LOS displacement over a wavelength of 6–8 km north from the splay fault, associated with post-seismic displacement on the splay fault. Though this interferogram spans the 9th November aftershock, there is no evidence of displacement in this line of sight. The TSX2 descending pass in-

terferogram shows a LOS displacement towards the satellite at the southern end of the profiles B, C, due to the 9th November aftershock, masking the effect of the splay fault. Superimposed on the aftershock deformation, we also see small discontinuities at both the VF and the BF (~ 1 cm). At both faults, all four interferograms

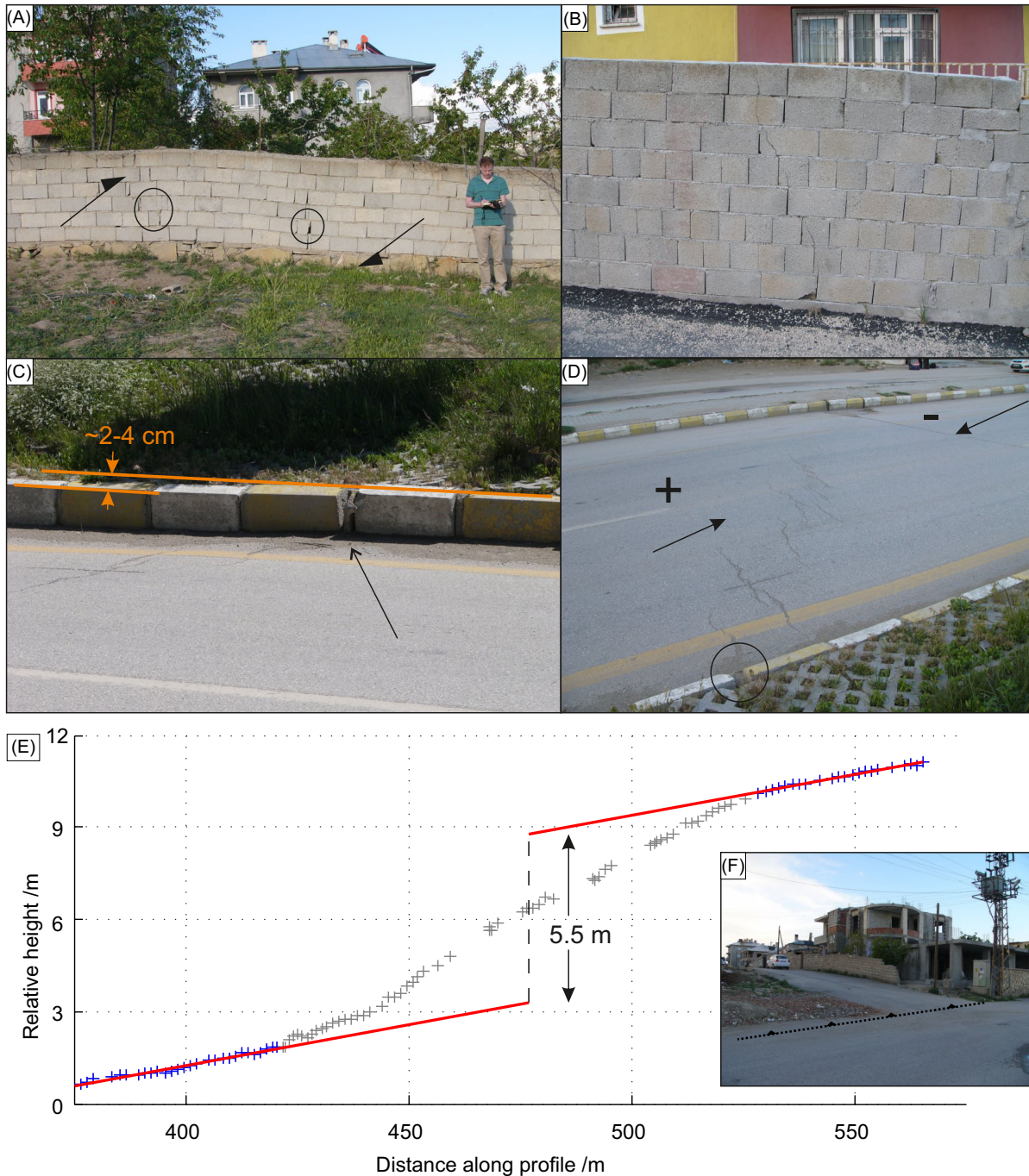


Figure 6. (a) Photo of a wall distorted by a few centimetres through post-seismic motion on the splay fault. The wall was constructed in 1993, but was undisturbed immediately following the earthquake. A tension gap and a cracked block are circled. Person for scale. Arrows indicate the sense of displacement of the wall. View east, location: 38.5283°N, 43.3472°E. (b) A second wall featuring cracks likely caused by the same post-seismic motion. The obvious crack has split individual blocks, but a second crack on the right has been repaired too. The orientation of these cracks is consistent with uplift on the north (left). View east, location: 38.5279°N, 43.3438°E. (c) Curb stones on the central reservation are displaced vertically, and gaps have developed between stones. The vertical displacement is ~2–4 cm. (d) Distorted tarmac on the Van–Erciş highway. Note that the displacement here has likely been exaggerated by the action of vehicles travelling over the displaced tarmac. Location (c and d): 38.5295°N, 43.3501°E. (e) Kinematic DGPS profiles across the scarp reveal a throw of $\sim 5.5 \pm 0.5$ m, Location: 38.5278°N, 43.3460°E. Points in grey were excluded from line fitting. (f) A view of a tarmac road ascending the scarp on the splay fault. On top of the scarp is a new building being rebuilt following the earthquake. Location: 38.5276°N, 43.3397°E.

show LOS displacement towards the satellite on the north block and away from the satellite on the south block, consistent with thrust or oblique left lateral fault slip.

The 9th November aftershock signal shows displacements of up to 4–5 cm LOS displacement in TSX2, but almost none in TSX1,

both of which span the earthquake. However, the USGS bodywave mechanism for the aftershock has a strike-slip mechanism with a small oblique component, on an approximately E–W or N–S striking fault plane. A simple elastic half-space model (Okada 1985), resolved into the look direction shows that for the north dipping,

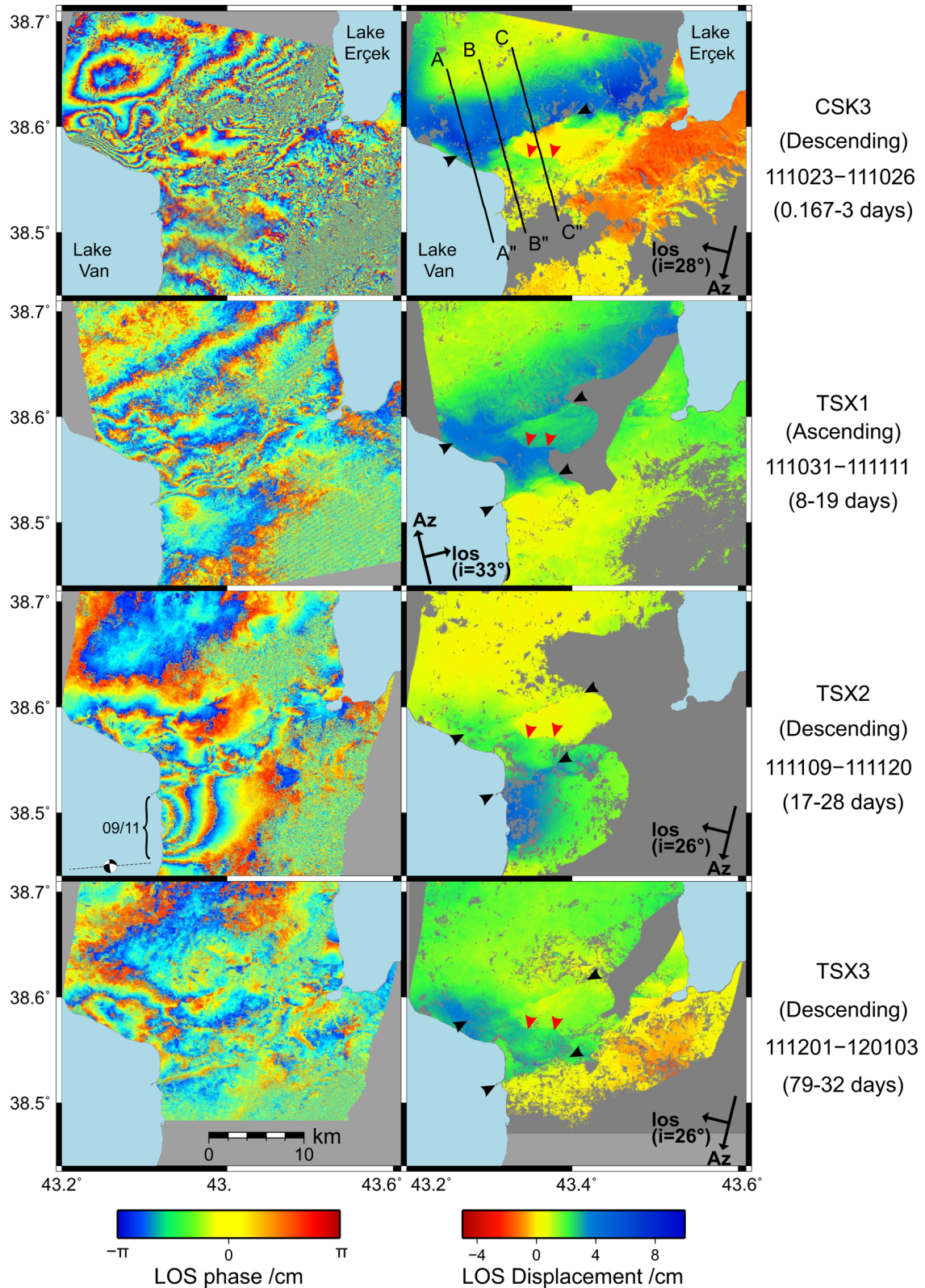


Figure 7. Series of COSMO-Skymed and TerraSAR-X interferograms for the period up to 2.5 months after the main shock, in temporal order top to bottom (outline shown in Fig. 2). Both the wrapped phase (left) and unwrapped interferogram (right) are shown—unwrapped LOS displacement is positive towards the satellite. We see clearly delineated both the Van and Bostaniçi faults (black arrows), along with a small backthrust (red arrows). There is a general uplift signal across the 5–8 km region associated with topography, with discontinuities at both faults. The locations of the profiles A–C of Fig. 8 are shown on the top right. The two middle interferograms (TSX1 and TSX2) also capture the edge of the displacement field for the 2011 November 9 M_W 5.9 aftershock near the edge of Lake Van (as identified by Doğan *et al.* 2014).

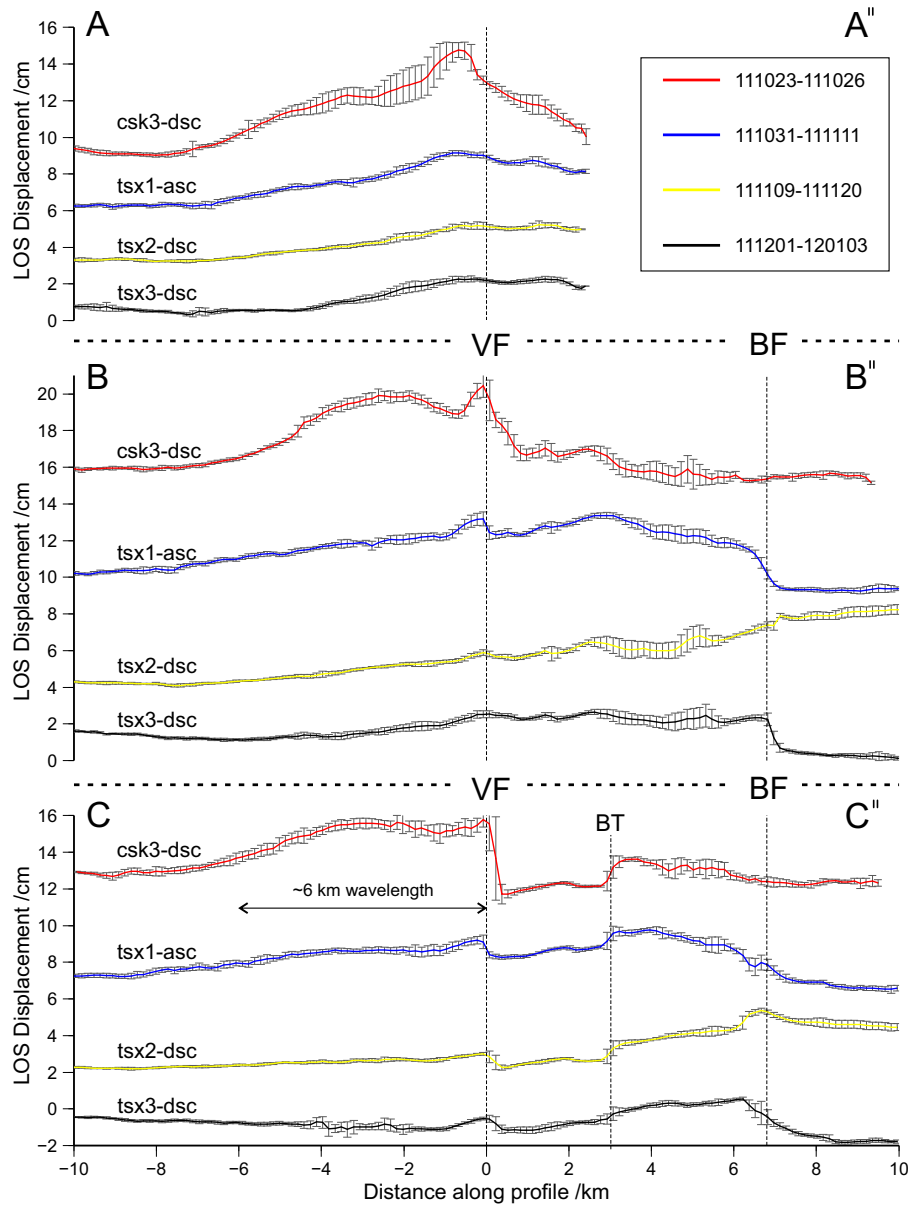


Figure 8. Profiles across the Van and Bostaniçi faults through the post-seismic interferograms in Fig. 7. LOS displacement is positive towards the satellite. Error bars represent the one sigma standard deviation in values of the points across the 1.5 km swath width of each profile, with the data binned in 100 m increments along profile. Note, a constant offset has been applied to each profile for clarity. Labels: VF, Van fault; BF, Bostaniçi fault; BT, Backthrust.

right lateral slip fault plane, the expected surface deformation pattern matches closely that observed, with very little motion in LOS for the TSX1 look direction, but significant motion in the TSX2 line of sight. Thus it is likely that the M_w 5.7 on 9th November occurred on a north dipping fault plane off the shore of Lake Van near the town of Edremit, though the fringes we observe suggest a location closer to Van city than the published seismological locations from the USGS and Irmak *et al.* (2012). This is consistent with the model of Wang *et al.* (2015) based on the TSX1 and ASAR2 interferograms.

Another common feature of all the interferograms is a small discontinuity between the VF and the Bostaniçi splay fault in profile C–C'', south side uplifted. This feature appears in both the wrapped and unwrapped interferograms (Figs 7 and 8), so we suggest that it is a small backthrust accommodating the transfer of motion between the two faults. There is no geomorphic signature

associated with this structure however, so we expect it to be a minor feature.

In summary, the sequence of interferograms show early shallow slip on the upper section of the VF resulting in uplift over a wavelength of ~ 6 – 7 km that is well correlated with the hanging-wall topography, but decays very rapidly over the days to weeks after the main shock. This is followed by an aftershock under the easternmost edge of Lake Van, for which the interferograms show motion consistent with right-lateral strike-slip/oblique faulting on an offshore fault near Edremit, striking E–W and dipping to the north. Either shortly before or following this aftershock, we observe creep on the BF. Superimposed is the continued creep on the VF at shallow depths (1–2 km). The final interferogram shows that both faults were still moving aseismically at least until the start of December (+39 d), though more slowly than in early interferograms (~ 1 cm over the 1 month period). The signal associated with the VF has a

wavelength of only ~ 1 km, so only very shallow motion remained in this period, whereas the signal associated with the Bostaniçi has a wavelength of ~ 6 km suggesting deeper slip was still continuing over the final period. Both faults show a slightly longer wavelength signal in the west suggesting that deeper slip was occurring there in all four interferograms.

Akinci & Antonioli (2013), Moro *et al.* (2014) and Wang *et al.* (2015) estimated the Coulomb stress changes on the fault planes of the 9th November M_W 5.7 aftershock predicted by the centroid moment tensor solutions; they suggest that the aftershock fault may have been brought closer to failure by the main shock as the transferred stress values generally exceeded 1 bar for both possible fault planes. The fringes associated with this aftershock in TSX2 suggest a centroid location significantly north and east of the USGS location. This suggests that the stress transfer values of Moro *et al.* (2014) and Akinci & Antonioli (2013) are likely to be underestimated, making it even more likely that the aftershock was triggered by stress transfer following the main shock.

4.3 Post-seismic slip: summary

Projecting the field measurements into satellite LOS, the offset at the Van–Erciș highway is equivalent to 14 cm towards the satellite for the descending pass interferograms (CSK3, TSX2, TSX3) and 4 cm away from the satellite for the ascending pass (TSX1). However, TSX1 displays motion towards the satellite in the hanging wall, suggesting that the large lateral offset may partly be a local site effect. This echoes the findings of Elliott *et al.* (2013) and Emre *et al.* (2011) who noted that the strike-slip:dip-slip ratio at the highway was much larger than was seen at most other locations. The descending interferograms are less sensitive to the lateral component, so we can still compare the observed thrust offset to the InSAR data. The CSK3 interferogram for the period of 4 hr – 3 d after the main shock shows an offset of ~ 4 cm at the highway, almost a third of the total measured in 2014, while the later interferograms show decreasing offsets of 2–0.5 cm over longer temporal baselines (finally, 0.5 cm over the period 39–72 d), suggesting that the aseismic slip-rate at the surface decayed very rapidly over at most the first 8 d.

At the BF, projecting the field measurements into radar LOS, we expect displacements of at most ~ 5 cm, which is less than the cumulative displacement measured in the interferograms (which do not cover the full time period). This is most likely because the surface displacement is more diffuse on this fault, with only a proportion localized at the pre-existing scarp—the InSAR profiles are generally smoother across this fault, with a length scale of 100–200 m.

5 GEOLOGICAL SLIP RATE

5.1 Overview

As noted above, the post-seismic surface breaks on the main VF and the BF were superimposed on pre-existing fault scarps. The surface trace of the VF bounds the southern margin of a range of east–west striking hills with a steepened southern slope, rising up to ~ 900 m above the level of Lake Van (Fig. 3). The relief is highest in the east, tapering down to the lake level in the west. These hills form an anticline in the hanging wall of the fault, with a wavelength of ~ 7.5 km (further discussion in Section 6.1). Many sections of the Late Quaternary fault scarp have been strongly altered by human

influence, but we identify several points where clear Quaternary scarps are visible, with heights of ~ 3 – 20 m. Both the fault and the range it bounds are characterized by two distinct geomorphic segments, an eastern and a western segment (Fig. 9).

The eastern segment of the VF extends from $\sim 43.44^\circ\text{E}$ to Lake Erçek, though lack of surface observations in the lake make it difficult to determine how far under the lake the fault extends and the rupture continued. This segment is characterized by a continuous scarp of typically ~ 30 – 50 m, consisting of an uplifted bedrock terrace (Fig. 9d). The fault trace is shown in Fig. 9a—there is a clear change from incision to deposition in crossing from the hanging wall to the footwall, but no coseismic surface displacements were observed in this section. During our brief field survey we did not find any Quaternary sediments on the terrace surface suitable for determining a slip-rate, but the well preserved, extensive and large scarp suggests it is likely that the fault extends to the surface in this segment. The relief associated with this section of the fault rises to ~ 900 m above the level of Lake Van, and is flanked by Pliocene sediments on the backlimb of the fold in several locations (see Section 6.1).

The western segment of the VF extends from the shore of Lake Van to $\sim 43.44^\circ\text{E}$ (Fig. 9). It is unclear whether the fault continues under the lake, though the decrease of the hanging-wall relief suggests that the fault ends near the edge of the lake. This asymmetry is not seen in the coseismic displacement field, suggesting that the fault may be growing westwards. This western section of the fault has cut through a series of the Quaternary alluvial and lake deposits, forming a semi-continuous range-front scarp. The scarps are developed primarily in volcanoclastic alluvial deposits and lacustrine deposits. They have generally been modified by agriculture, but we found a number of sites where the scarps are well-preserved. The three sites (S1, S2 and S3) that we selected for slip-rate measurements, where we see scarps of ~ 3 m, ~ 5 m and ~ 18 m respectively, are shown in Fig. 9. We use a combination of optically stimulated luminescence (OSL) dating and radiocarbon dating to estimate the deposition age of two surfaces at sites S2 and S3. We use kinematic DGPS and SfM to generate digital elevation models of the scarp in two separate locations, and DGPS profiles in a third, to estimate fault throw at the surface.

5.2 Slip-rate measurements

5.2.1 Site S1

The VF continues eastwards along strike of the deformation of the Van–Erciș highway (described in Section 4.1) as a low scarp tracking across agricultural fields (Fig. 10a). Despite significant ploughing having occurred, the scarp is clearly visible in the Late Quaternary volcanoclastic alluvial sands and gravels with a 10–20 cm soil developed at the surface. DGPS profiles across the scarp show 2.7 ± 0.3 m of vertical throw (Fig. 10b). Quartz OSL samples collected from a pit in the upthrown side of the scarp have unfortunately not been possible to date due to the insensitivity of the quartz. It is however still clear that at site S1 significant Late Quaternary fault slip has reached the surface to generate the scarp.

5.2.2 Site S2

Immediately east of site S1, the land has been heavily modified by building, but ~ 2 km further east, at site S2 (Fig. 9), we found further scarps in similar materials (Fig. 11a). We use SfM (see Section 3)

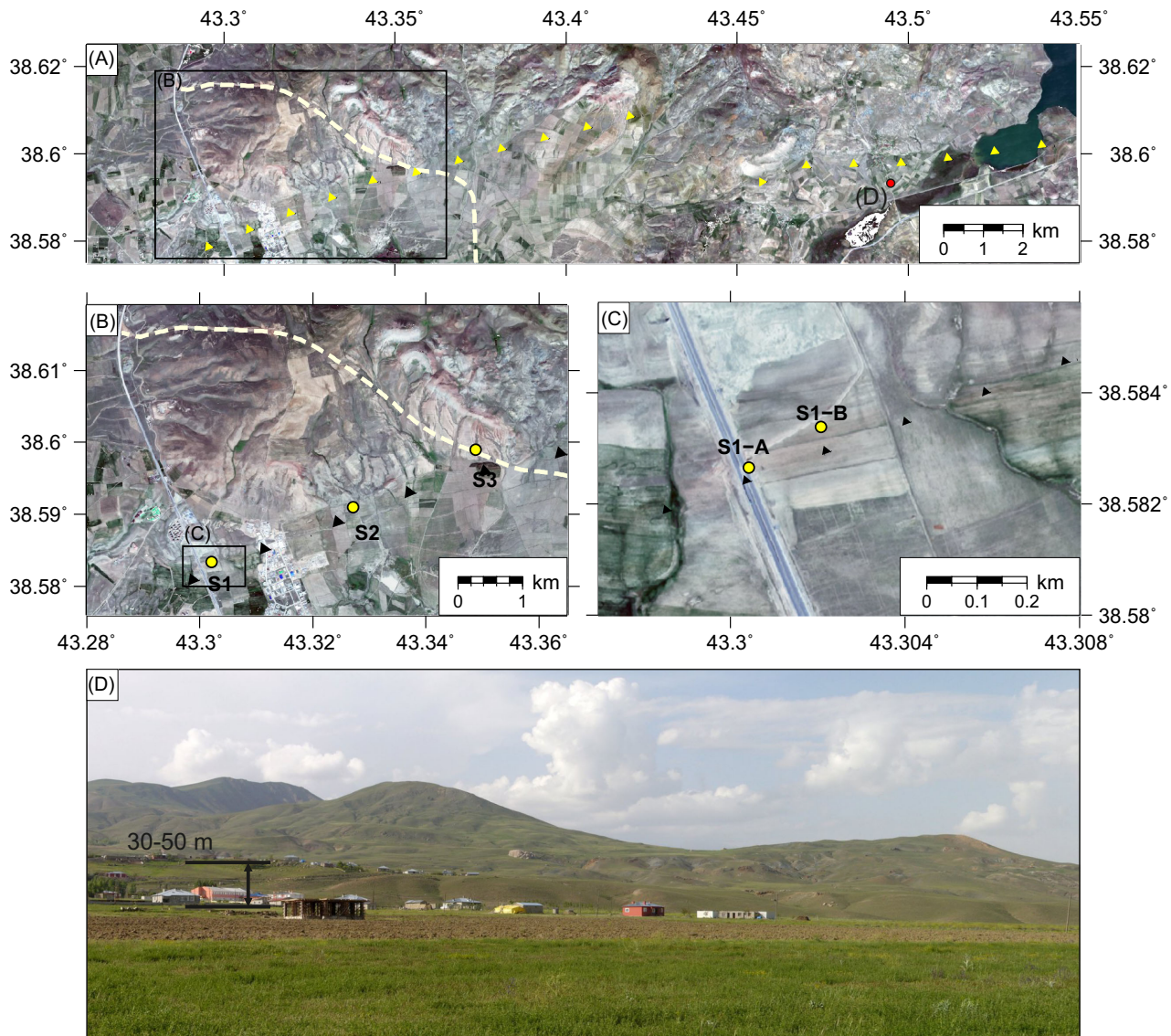


Figure 9. WorldView-2 Multispectral RGB true colour 0.5 m pansharpened imagery of the Van fault (May–June 2011). (a) An overview of the Van fault showing both the eastern and western segments, denoted by yellow arrows. In the east, the scarps are primarily bedrock, but in the west they cut Quaternary sediments. (b) The western section of the scarp, with the three field sites discussed in Sections 5.2.1–5.2.3 shown in yellow, and the new highway, which provides the cutting for sampling at S3, shown as a dashed line. (c) Close up of the site S1, divided into two, S1-A - the road cutting in which we see a fault exposure and displaced pavements (Fig. 4), S1-B a shallow scarp of 2.7 ± 0.3 m in Quaternary deposits (Fig. 10). (d) Photograph of the ~ 30 –50 m bedrock scarp of the eastern segment of the Van fault, near lake Erçek. Photo looking north, location: 38.5948°N , 43.4943°E .

to quantitatively assess topography of this site, using photographs from a digital camera mounted on a 6 m pole, to create a DEM of a 200 m stretch of the scarp (Figs 11c and d). Fitting parallel planar surfaces to the pointcloud above and below the scarp, we measure a vertical offset of 4.7 ± 0.3 m on this section of the scarp (Fig. 11e).

We collected two OSL samples from the upthrown side of the scarp to date the deposit (OSL5 and OSL6 in Table 3, Fig. 11b, OSL measurement protocol described in Section A). These two samples give close agreement at 9.0 ± 2.7 ka for the age of the offset surface. However, as we discuss in Section 5.2.3, the quartz OSL in the region is generally dim for all samples and does not agree well with radiocarbon dating at site S3, so we are cautious in our interpretation of these dates.

5.2.3 Site S3

Site S3 is situated 2 km east of S2 (Fig. 9a). Here the fault is expressed as a much larger cumulative scarp within a series of alluvial fans, as shown in Fig. 12(a). A vertical throw of 18 ± 1 m was measured at this site from multiple DGPS profiles (Fig. 12b). Our measurement of vertical displacement neglects footwall sedimentation since surface abandonment, so the offset measurement here is considered a minimum fault throw since the abandonment of the upthrown surface.

The hanging-wall deposits again consist of volcanoclastic alluvial sands and gravels which are well exposed in a new road cutting (Fig. 12b). Most of the deposits are composed of well-rounded clasts up to ~ 10 cm, consistent with a high-energy alluvial setting.

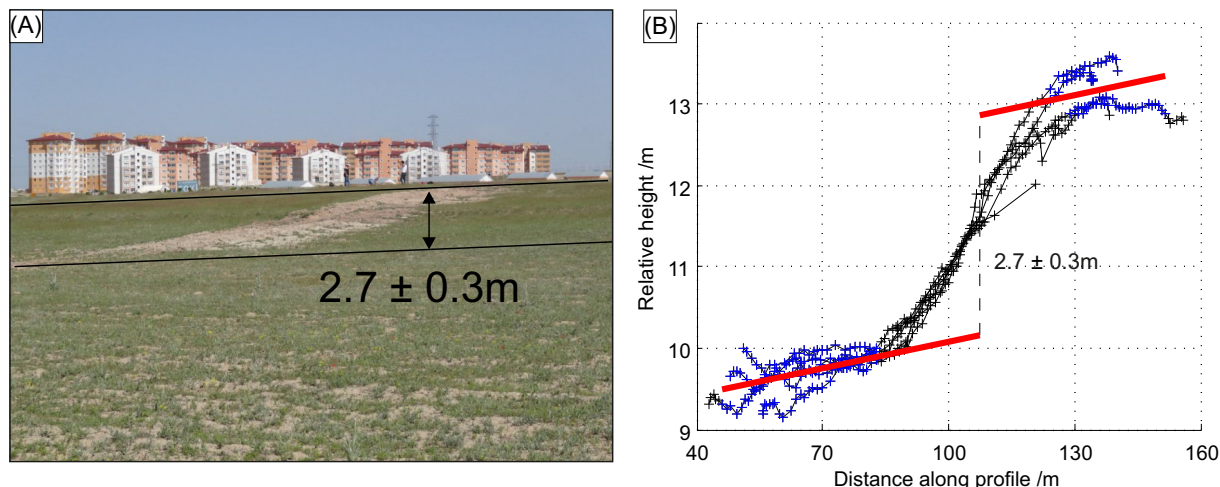


Figure 10. (a) At site S1b, near the main road we observe a 2.7 m scarp in Quaternary material. Immediately behind the scarp, new apartment blocks have been constructed on the hanging wall of the fault, built after the earthquake to replace some of the damaged building stock. Photo looking NW from 38.5826°N , 43.3029°E . (b) Four stacked kinematic DGPS profile across the scarp at S1, showing an offset of $2.7 \pm 0.3\text{ m}$. Points in black were excluded from line fitting.

However, we also found a few localized deposits consisting of fine-grained sand and silt. The fine-grained deposits were laminated in places, and contained abundant freshwater gastropod shells. The fine-grained units were interbedded within the gravel deposits and, due to their restricted extent, we interpret them to have formed as small ponds perched on the aggrading alluvial fan surface.

We collected three OSL samples (OSL1, OSL2, OSL7 in Table 3) and several gastropod shells for radiocarbon dating (Table 4) from the fine-grained units. The sampled gastropod shells were found in a single continuous layer in an undisturbed stratigraphic sequence, suggesting they were living in place prior to an extinction event—it is unlikely that they were transported there after death of the organisms. The shells yield a mean calibrated radiocarbon age of $44.0 \pm 2.0\text{ ka}$ (Shell_A, Shell_B and Shell_C in Table 4). Each sample represents an individual shell and the individual probability density functions based on the IntCal13 calibration (Reimer 2013) are shown in Fig. 12(d). The OSL samples give ages of ~ 7.0 , 7.2 and 11.1 ka (Fig. 12), which are much younger than the radiocarbon ages obtained from the same outcrop. We attribute the mismatch to low sensitivity of the quartz to OSL (e.g. Rhodes 2015). Low quartz sensitivities have been found in studies in nearby Iran, similarly resulting in anomalously young burial ages (Fattahi *et al.* 2007; Walker & Fattahi 2011). The low quartz content also reduced measurement reliability due to a small quartz sample size.

5.2.4 Slip-rate estimates: summary

Taking the mean radiocarbon age at Site S3 as a reasonable bound on the age of the displaced surface we calculate a minimum throw rate of $0.4 \pm 0.1\text{ mm yr}^{-1}$. Fig. 13 shows a plot of offset against age for each of the samples at site S3, with a line indicating an uplift rate of 0.4 mm yr^{-1} , calculated based on the mean radiocarbon age at Site S3. The two OSL ages from site S2 (OSL 3 and 4) are consistent to within error of this line, suggesting that those two samples ages may be reliable, though as we have no independent age constraint on the sediments at site S2 we cannot confirm it.

We note that $0.4 \pm 0.1\text{ mm yr}^{-1}$ is a minimum bound on the throw rate, as the measured offset assumes no post-formation deposition in the footwall of the scarp, and we do not account for any folding or off-fault deformation occurring in the near-surface. Taking the

fault dip of 45° – 50° as estimated from the road cutting on the Van–Erciş highway (consistent with the InSAR solution, though this may differ from the shallow sub-surface dip), we find a minimum fault slip-rate of $0.5 \pm 0.2\text{ mm yr}^{-1}$.

6 DISCUSSION

6.1 Fault geometry

The co-seismic geodetic models for the 2011 main shock broadly agree, but there are a few key differences. The solution from Elliott *et al.* (2013), based on the earliest co-seismic pair (10/10/2011–23/10/2011, CSK1 in Table 2), shows no clear discontinuities at the surface and gives evidence for two fault segments, with only the lower sections (below 10 km) failing in the earthquake. The west/east segments strike approximately east–west and dip at $40^\circ/55^\circ$, with top depths of 10/8 km and bottom depths of 19/17 km respectively. In their distributed slip model, they resolve a strong up-dip gradient in slip, suggesting an abrupt arrest at the upper limit of rupture at $\sim 10\text{ km}$. The up-dip projections of the two fault segments are tied to the location of small ground displacements mapped in the field, so the geometry is not entirely free, though the authors note that their tied location gives a minimum misfit to the data. The coseismic model of Wang *et al.* (2015), combining all of the available geodetic data, finds a similar two-fault geometry, with two distinct patches of intense slip up to a maximum of $\sim 6.3\text{ m}$.

Fielding *et al.* (2013), Moro *et al.* (2014) and Feng *et al.* (2014) instead prefer single fault models for simplicity and lacking primary surface ruptures to tie segments to. These models incorporate additional azimuthal displacements from multiple aperture interferometry (MAI) or amplitude image pixel correlation. They show slip and significant moment release is restricted to depths below ~ 6 – 8 km , consistent with a high density of aftershocks at this depth due to a strong slip gradient. Feng *et al.* (2014) present the CSK1 coseismic interferogram, which includes only the first 4 hr of the post-seismic period. In contrast, the CSK2 interferogram used by Fielding *et al.* (2013) and Wang *et al.* (2015) includes the 3 d following the main shock, during which time a significant (M_w 5.9) aftershock occurred in the epicentral region and significant shallow post-seismic slip occurred (Section 4). Thus, their coseismic

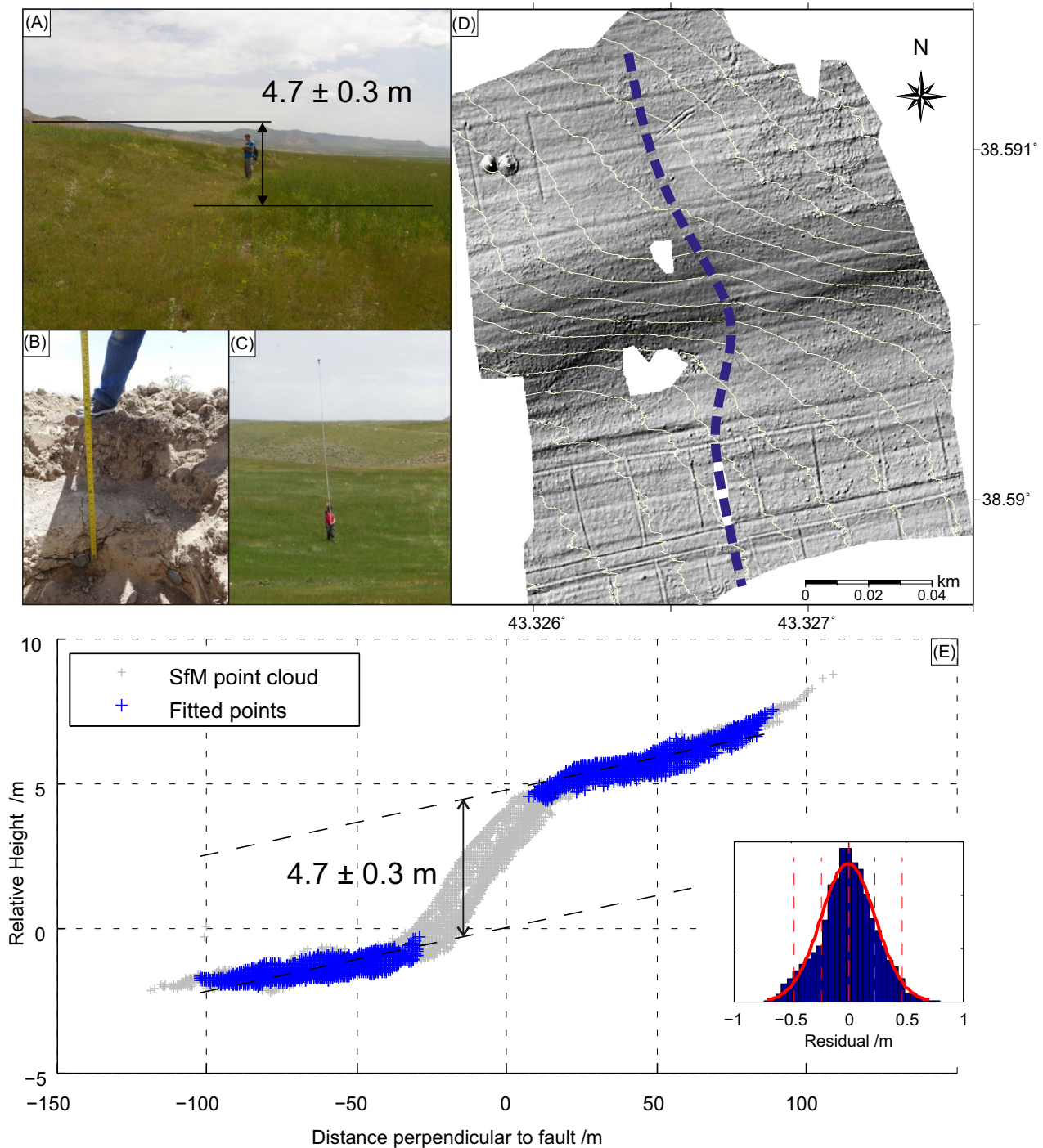


Figure 11. (a) Scarp visible at Site S2 running through agricultural fields, person for scale. Photo taken looking E at 38.5909°N , 43.3282°E . (b) Sample pit at S2 in the hanging wall, two OSL samples (OSL5 and OSL6, Table 3) collected from a depth of 58 cm. (c) Compact digital camera mounted on a 6 m pole to collect photographs for structure from motion. (d) Shaded relief DEM of a 200 m stretch of the scarp at the S2 site, overlaid with 1 m contours, generated from ~ 1100 photos by SfM. The horizontal banding in the image represents the individual plough furrows and irrigation channels of the agricultural field. Three small patches with poor photograph coverage have been masked out. The small channel (dashed blue line) running through the middle of the scarp has also been masked out for the purpose of measuring an offset. (e) The fault throw here was measured by fitting parallel planes in the hanging wall and footwall and measuring the vertical offset between them. This plot shows the points projected along the plane into a fault perpendicular profile. The inset shows the residuals to fitting the planes, compared to a Gaussian of the same mean and standard deviation. We find rms misfits of 0.22 m and 0.25 m for the footwall and hanging wall respectively, giving an uplift of 4.7 ± 0.3 m. Points in grey were excluded from plane fitting.

models will contain a small amount of post-seismic slip as well as the main shock coseismic slip. We note that studies using the CSK2 interferogram consistently estimate a larger coseismic moment release than those modelling the CSK1 interferogram (Table 1), likely

due to the inclusion of a large fraction of the total post-seismic motion.

Similarly, the seismological models broadly agree. Modelled source-time functions from low-frequency teleseismic data are

Table 3. Table of Optically stimulated luminescence (OSL) dates. The vertical throw for each site (locations in Fig. 9) is also shown.

Name	Sample	Site	Site offset (m)	Offset error (m)	Age B.P. (ka)	Age error (ka)
OSL3	X6333	S1	2.7	0.3	fail	–
OSL4	X6334	S1	2.7	0.3	fail	–
OSL5	X6335	S2	4.8	0.5	9.2	2.6
OSL6	X6336	S2	4.8	0.5	8.9	2.6
OSL1	X6331	S3	18	1	7.2	2.3
OSL2	X6332	S3	18	1	7.0	1.5
OSL7	X6337	S3	18	1	11.1	4.0

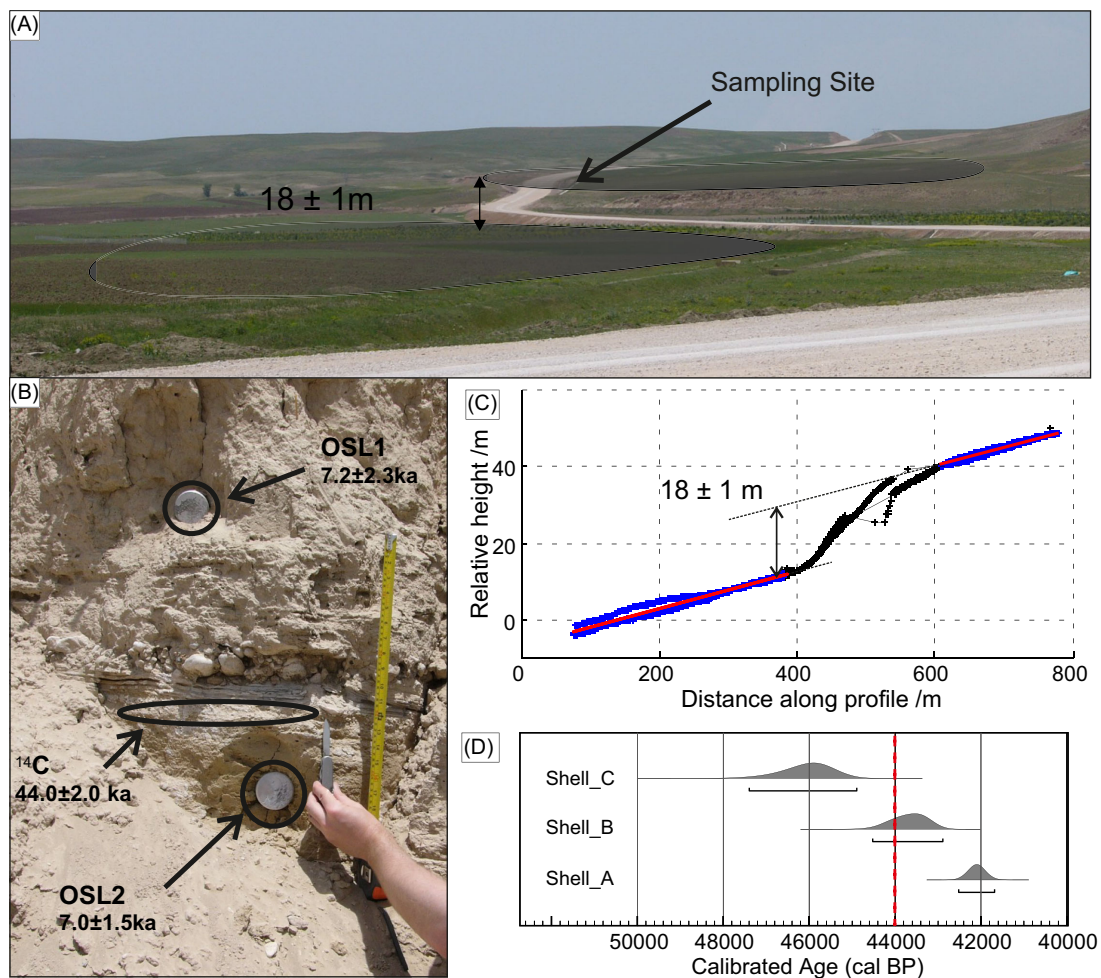


Figure 12. (a) Larger scarp at site S3, with a minimum throw of ~ 18 m. This location provides the main basis for our preliminary slip-rate. Photo taken looking NW from 38.5874°N , 43.3732°E . (b) Setting of the two OSL samples and gastropod shells (^{14}C) found at site S3. The two OSL samples are from fine grained silt beds above and below that containing the gastropod shells. Note the presence of the occasional gravel layer interspersed, suggesting the presence of occasional higher energy flows. The gastropod shells (including Shells A–C listed in table 4) are found in abundance in a sandy layer beneath silt and gravel beds. The abundance of shells suggests that are unlikely to have been redeposited. (c) Three stacked DGPS profiles used to estimate the minimum offset on this surface. Points in black were excluded from line fitting. (d) Radiocarbon ages for three shells from the same horizon at site S3. Dates are presented using the OxCal program V4.2 (Bronk Ramsey 2009), and calibrated using the IntCal13 atmospheric curve (Reimer 2013). Dashed line represents the unweighted mean age.

Table 4. Radiocarbon ages for the three gastropod shell samples collected from site S3 (Fig. 9b). Ages calibrated using the IntCal13 atmospheric curve (Reimer 2013).

Sample	Conventional age (ka)	1σ Error (ka)	$\delta^{13}\text{C}$ ‰	Calibrated age B.P. (ka)	95 per cent confidence interval (ka)
Shell_A	37780	280	1.5	42100	420
Shell_B	39990	460	0.4	43710	820
Shell_C	42710	620	-0.1	46140	1250

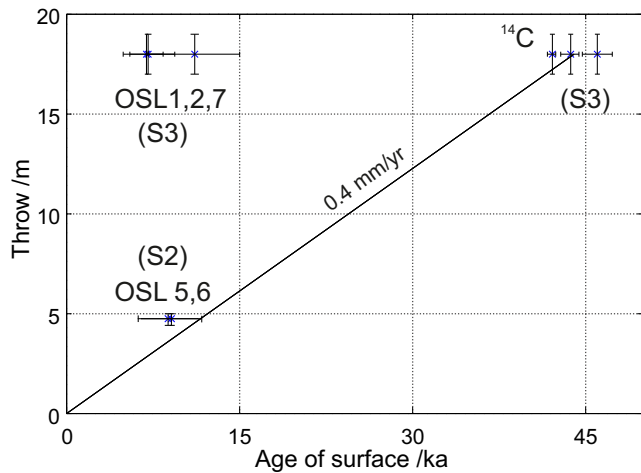


Figure 13. Vertical offset against age for each of the samples. Line represents an uplift rate of 0.4 mm yr^{-1} that we get using the Site S3 ^{14}C sample only. Note that this line is consistent to within error of the OSL ages observed for site S2 (OSL 5,6).

generally triangular with a total length of 10–15 s, though the position of the peak varies between models (Zahradnik & Sokos 2011; Elliott *et al.* 2013; Fielding *et al.* 2013). Using a higher frequency range with regional to near-regional stations and a multiple point source model, Gallovic *et al.* (2013) and Zahradnik & Sokos (2014) resolved a source-time function consisting of two distinct sub-events separated by 3–4 s, with locations corresponding well to the two fault segments resolved with InSAR by Elliott *et al.* (2013). Finite fault models by Irmak *et al.* (2012) and Fielding *et al.* (2013) show close agreement in the source time functions, with the majority of the moment released in a triangular source-time function spanning the first 10 s, and a subsidiary peak at around 14–15 s. Using backprojection of strong motion waveforms, Evangelidis & Kao (2013) image two distinct sources of high frequency radiation at depths of 10–12 km in locations corresponding well to the two fault segments, which are attributed to stopping phases or rupture propagating through geometric complexities (possibly linking between the two fault segments).

The seismological and geodetic models agree that coseismic slip does not extend to the surface, with little significant moment release above depths of 7–10 km. In addition there is strong evidence for geometric complexity, with the two-fault models giving a good fit to the SAR data and two discrete pulses of slip observed in the source time functions and multiple-point source models.

Fig. 14(a) shows an overview of the VF and surrounding structures. From the large-scale topography it appears that the main VF and the BF merge to form a single trace in the east, consistent with the model of Wang *et al.* (2015). In the west, the two faults are characterized by a footwall basin and a narrow range of hills in their immediate hanging walls, which we attribute to folding of the hanging wall. In both ranges, we see a series of prominent windgaps likely resulting from earlier drainage across the folding axis. Approximately 7 km north of the VF, near the village of Satbey, we observed back tilted Pliocene sedimentary units (MTA 2002) dipping north at $\sim 20^\circ$ (Fig. 14b). However, ~ 1 km further north across the valley, the same Pliocene sediments are horizontal. The wavelength of folding therefore stretches ~ 7.5 km north from the fault, corresponding closely to the observed topography (Figs 15a and b).

The coseismic uplift associated with the 2011 earthquake was distributed over a wavelength of 20–25 km, much wider than the hanging-wall uplift preserved in the large-scale topography (Fig. 15a). It is unlikely, therefore, that repeated earthquakes of the style of that in 2011 are responsible for generating the hanging-wall topography. Discrete slip on the deeper section of the VF in 2011 must give rise to a deficit of slip in the uppermost 8 km, and our observations of Quaternary scarps at the surface suggest that at least some of this motion is localized onto the two faults. By contrast the topography and wavelength of folding at the surface is closely correlated with the observed post-seismic displacement (CSK3). This suggests therefore that displacement in the upper ~ 8 km is responsible for the observed topography; a simple 2-D elastic half-space model (Fig. 15a) gives a good fit to the CSK3 profile, with 8 cm of slip on a 55° dipping fault plane (0.6–7 km depth). It is likely, however, that some of this topography is due to fold growth, so a 2-D elastic model may not be entirely appropriate. Indeed, scaling this model to the observed topographic relief gives net rotations of $< 1^\circ$ near Satbey, so to achieve the observed Pliocene bed rotations over the 7–8 km wavelength, significant anelastic off-fault deformation must also occur.

Fig. 15(c) presents our schematic model of the VF, which builds on a model produced by Doğan *et al.* (2014), in which we have brought together our observations from the co-seismic and post-seismic InSAR, field observations of surface faulting, and of long-term folding observed in the topography and bedrock geology. Our model is for a profile orthogonal to the western segment of the VF in order to compare results with our Late Quaternary slip rate (Section 5.2). The model consists of a $\sim 45^\circ$ N-dipping reverse fault within the depth range of 8–25 km, which steepens at a depth of ~ 7 –8 km beneath the northern edge of the observed fault related topography. The steeply dipping VF reaches the surface at the observed Quaternary scarps and small post-seismic surface displacements, while the splay follows a shallower dipping detachment to steepen under the northern edge of Van city, reaching the surface where we observe further post-seismic displacements. We mark the splay fault dashed as, although it is likely to meet the main VF at depth, the precise depth at which it does is poorly constrained. The change in dip at depth on the VF (possibly the same depth at which the fault splays) may have provided a barrier to rupture propagation during the 2011 earthquake, consistent with the observations of Doğan & Karakaş (2013), Elliott *et al.* (2013), Fielding *et al.* (2013), Feng *et al.* (2014) and Wang *et al.* (2015) who all observed a strong slip gradient and rupture termination. This is also consistent with Evangelidis & Kao (2013) who imaged a high-frequency (HF) source at this depth and location which they relate to rupture termination or geometric complexity. A similar trend was observed in the location of the HF seismic radiation sources in the 2015 Gorkha Earthquake, Nepal (Avouac *et al.* 2015); Elliott *et al.* (2016) show that the HF sources are co-located with a change in dip of the fault plane, though in that case, they were in the middle of the rupture zone.

6.2 Post-seismic motion

Combining field observations with quantitative measurements from the post-seismic InSAR interferograms, we have evidence of shallow, post-seismic creep on both the VF and the BF, consistent with previous estimates of post-seismic motion imaged with GPS (Altiner *et al.* 2013; Doğan *et al.* 2014) and InSAR (Elliott *et al.* 2013; Fielding *et al.* 2013; Feng *et al.* 2014; Moro *et al.* 2014; Wang *et al.* 2015). The main shock occurred on the VF, which breaks the

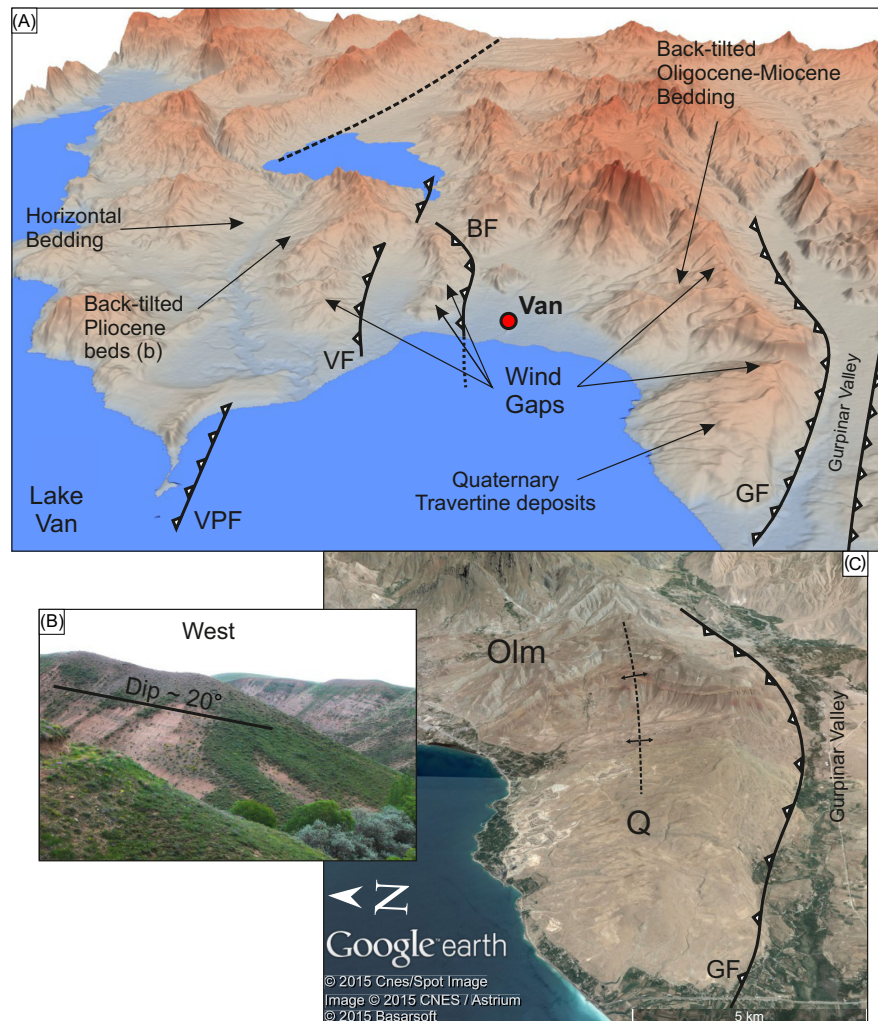


Figure 14. (a) 3-D perspective view looking east along the Van fault and the Bostanci fault. Also marked are the Gürpınar (GF) and Peninsula (VPF) faults. Arrows indicate the location of several prominent windgaps in the ridges and folded sedimentary units. (b) Back tilted Pliocene beds near the village of Satbey, dipping $\sim 20^\circ$ N. Photo looking west, location: 38.6843° N, 43.4823° E. (c) Oblique view of the Quaternary Travertines (labelled in (a)) and folded Oligocene-Miocene sediments in the hanging wall of the Gürpınar thrust.

surface ~ 8 km north of Van, but Doğan *et al.* (2014) and Wang *et al.* (2015) use post-seismic regional GPS and TerraSAR-X data (TSX1 and TSX2, Table 2) to identify a second, splay fault (the BF), which reaches the surface in the northern suburbs of Van. Thus, in the weeks following the main shock, a small amount of slip reached the surface, both at the surface projection of the main VF, and on the splay fault ~ 7 km to the south. Doğan *et al.* (2014) also identify fringes in the TSX1 and TSX2 interferograms relating to the M_W 5.9 aftershock on 9th November (strike-slip mechanism). Wang *et al.* (2015) go further to model slip on both faults based on the time-series of TSX scenes—estimating as much as 0.7 m of slip.

Post-seismic surface displacement due to slip on the VF occurs over a wavelength of ~ 6 – 7 km—the simple 2-D forward model for fault slip on the upper VF closely matches the observed post-seismic surface displacement (Fig. 15a), suggesting the creep is confined to the upper, largely locked section of the VF. This is in agreement with the suggestions of Wang *et al.* (2015) and Altiner *et al.* (2013) who find that the majority of the post-seismic motion occurs over a broader region than the coseismic rupture. Shallow post-seismic slip is also consistent with the observations of Acael *et al.* (2014)

from cross correlation of ambient seismic noise, which show a velocity decrease at the main shock that does not recover for the higher frequency bands which sample the shallower crust, suggesting continued shallow slip. Combining the observations from both CSK3 and the TSX scenes, we observe creep on the VF decaying over a very short timescale of hours to days, whereas the BF does not creep during the 3 d following the earthquake, but is clearly creeping following the M_W 5.7 aftershock, with a slower decay constant (evidenced by significant displacement in the TSX3 interferogram, more than 24 d after the aftershock). This is consistent with the suggestions of both Doğan *et al.* (2014) and Wang *et al.* (2015), that there was a time delayed migration in post-seismic motion from the VF plane onto the splay fault, possibly due to static stress change or fluid migration. We do not observe a longer wavelength signal that would suggest significant afterslip in the coseismic rupture region.

In the recent 2014 Napa Earthquake, significant rapid post-seismic motion was also shown to occur in the hours to days following the earthquake (e.g. Hudnut *et al.* 2014; Brocher *et al.* 2015), though the first post-event InSAR pass was not until 3 d after the event. Lienkaemper *et al.* (2016) estimate that up to around one quarter of total expected afterslip motion may have been taken

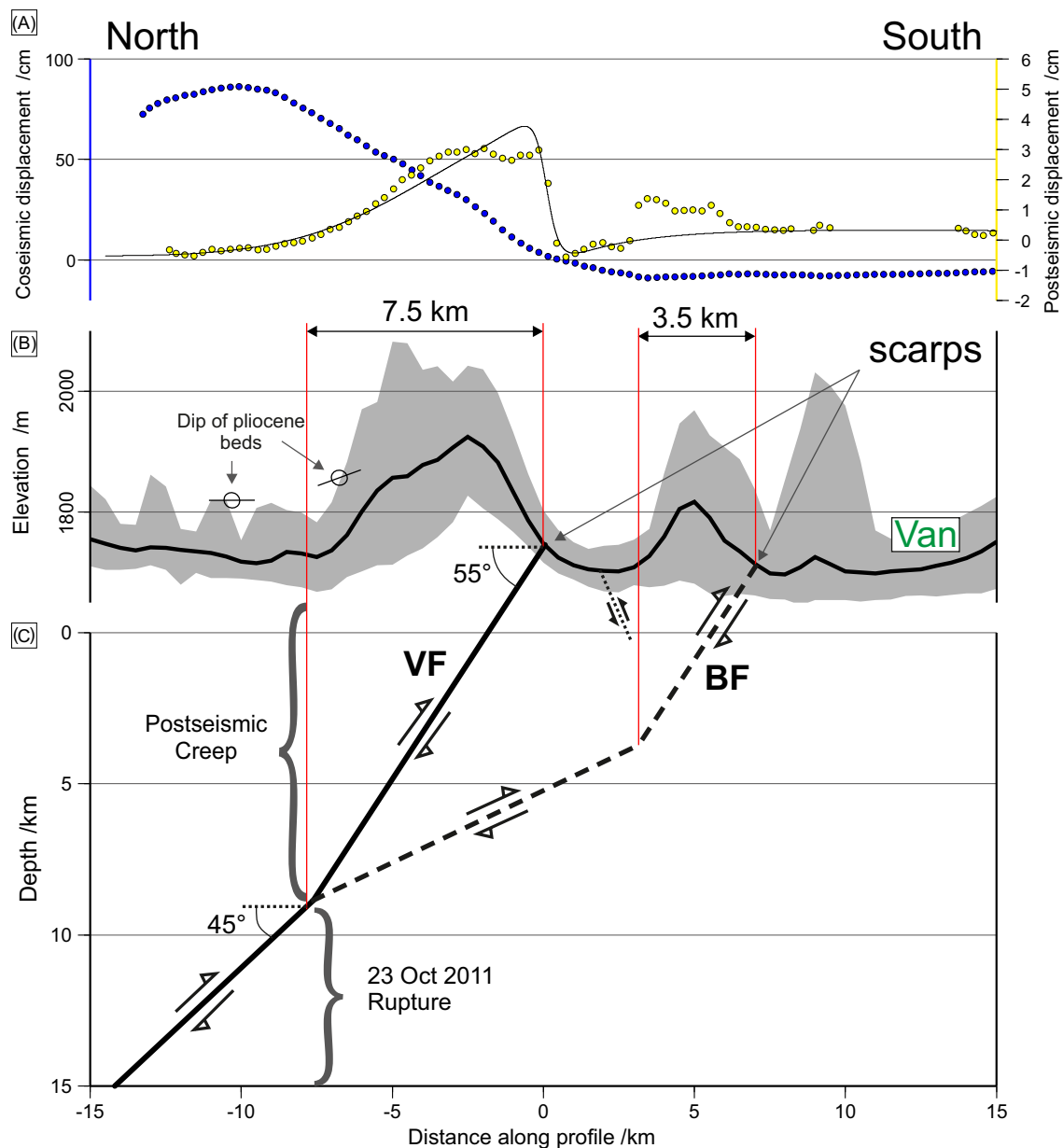


Figure 15. (a) Coseismic (blue, 10/10/2011–23/10/2011, CSK1) and early post-seismic (yellow, 23/10/2011–26/10/2011, CSK3) line-of-sight displacement profiles. The thin black line shows a simple forward model for 8 cm slip on the uppermost 7 km of the fault, closely fitting the wavelength observed in the post-seismic InSAR. (b) The same profile through SRTM topography, average elevation in black, with minimum/maximum bounds shaded grey. The locations of the tilted/undisturbed Pliocene units are also shown. (c) Structural cross-section based on the observed topographic wavelength associated with each fault north of Van. This transect is taken through the western segment of the fault where we observe two distinct faults, the Van fault (VF) and the Bostaniçi fault (BF).

up within the first day on some sections of the fault. Both the Napa and Van earthquakes have shown very rapidly decaying post-seismic motion after the event, declining over periods of hours to days. Inclusion of this short-term post-seismic displacement in InSAR-derived slip models could give systematic overestimates of coseismic moment release and shallow fault slip. In order to accurately characterize this shallow afterslip and to differentiate between coseismic and post-seismic slip, we need very rapid and easily deployed measurement techniques. Shortened revisit times with new radar satellites will improve InSAR capabilities (Elliott *et al.* 2015b), but post-seismic acquisitions are still likely to be multiple days after events instead of hours. We have shown that a single

person with minimal training can generate a DEM of a ~ 200 m area in under an hour with minimal cost—this can be achieved even faster with a small quadcopter or fixed wing drone as was performed by several teams following the Napa earthquake. Thus observations are limited only by time required to travel to the event location and re-visits can be near continuous. In the future, with the increase in availability of cheap and rapid observation, we expect to see much higher temporal sampling of post-seismic motion particularly in the acquisition of near zero-delay type observations, giving the chance to better constrain the evolution and behaviour of surface and near-surface faulting both in the coseismic and post-seismic phases.

6.3 Earthquake Hazard

We have imaged a post-seismic transient on the VF which decayed rapidly after the main shock, amounting to <20 cm of measurable aseismic fault slip. Transient slip on the Bostaniçi splay fault is also imaged, and likely decayed with time.

Wang *et al.* (2015) estimate up to 0.7 m (34 per cent of main shock moment) of post-seismic slip on the fault plane, over the first 3 months of the post-seismic period, and hence suggest that the fault does not represent significant future seismic hazard. Although we do not model the fault slip, the total surface displacements we observe amount to less than 15 per cent of those observed after the deeper main shock in the radar line of sight. The solution of Wang *et al.* (2015) requires larger lateral slip on the upper fault, which the InSAR measurements are less sensitive to, but there still remains a slip deficit if one considers the thrust component of slip. As such, the maximum thrust slip we estimate on both the upper VF and the splay fault in the earthquake and the first 2.5 months of post-seismic motion is still only a small fraction of the average slip modelled at depth (though a much longer time-series is needed to determine the full post-seismic behaviour). The two large, shallow aftershocks, combined with the presence of fault gouge at the surface (Elliott *et al.* 2013) suggests that the upper crust is capable of sustaining earthquakes, so the fault may represent significant seismic hazard to the region. Palaeoseismic trenching is required to characterize the earthquake behaviour of the upper fault. It is clear, however, that significant slip does reach the surface on a discrete fault plane ($\geq 0.5 \text{ mm yr}^{-1}$) and that the upper 8–10 km of crust is capable of sustaining earthquakes.

Considering the unruptured upper part of the VF, the fault length of ~25 km and a bottom depth of 10 km gives a fault plane of similar area to that which failed in the 2011 earthquake. Assuming the same average slip (~3.7 m, Elliott *et al.* 2013) modelled at depth (or equivalently that average slip scales with fault area e.g. Wells & Coppersmith 1994), would yield another earthquake of M_w 7.1. The slip would be equivalent to 2.6–2.8 m uplift at the surface (assuming a dip of 45–50°), suggesting that the scarp at site S3 is comprised of at least ~6–7 earthquakes, with recurrence intervals of <8 ka if the fault fails in characteristic earthquakes. It is likely however, that some of the slip at depth is accommodated as folding, giving rise to the anticlinal ridge that forms the hanging-wall topography (see Section 6.1, Fig. 14). An earthquake on the upper section of the fault would have a centroid 10 km shallower than the 2011 event, and would also be ~10 km closer to the city of Van, and hence would likely result in much heavier damage to the city than the 2011 earthquake.

The 2011 Van earthquake occurred on the fault below a depth of ~8–10 km, with a magnitude M_w 7.1. As discussed, the coseismic uplift does not correlate with the topography, and so the surface topography reflects the structure of the upper ~7–8 km of the crust. Thus the Van earthquake illustrates difficulties for palaeoseismic and geomorphic investigations in regions of thick skinned faulting, as we see that large ($M > 7$) earthquakes can be generated by deep ruptures which do not affect the surface geomorphology. The lack of primary surface ruptures also means that palaeoseismic trenches on reverse faults in the region can ‘miss’ earthquakes of at least M_w 7.1 and estimates of earthquake hazard in the region based on surface data will underestimate the depth extent of seismogenic faulting and hence maximum earthquake magnitudes.

Using the diagnostic features of uplift observed in the hanging walls of the VF and BF, we map several more faults across the region (see Fig. 2), complementing previous studies (e.g. Altinli

1966; Saroglu *et al.* 1992; Özkaymak *et al.* 2003; Karakhanian *et al.* 2004; Özkaymak *et al.* 2011; Üner *et al.* 2015). These include the Gürpınar fault to the south of Van city (Figs 14 a and c) on which we identify a series of wind gaps in the ridge line and north-dipping tilted sedimentary units on the backlimb (Quaternary Travertines and Oligocene–Miocene sediments). An earthquake on this fault would also be damaging to the city of Van, as the inferred north-dipping fault plane projects directly beneath the city given similar dip ranges. The Gürpınar fault ridge is ~50 km in length, longer than the VF, and from scaling relationships one could expect slip in even larger magnitude events to occur on this structure (Wells & Coppersmith 1994).

7 CONCLUSIONS

The M_w 7.1 Van earthquake involved rupture of a reverse fault over a depth range of 10–25 km and did not break the surface. The main shock was followed by post-seismic slip on two upper crustal splays above the seismic rupture. We suggest that a change in dip and possible splaying of the fault at a depth of 7–8 km created a structural barrier to propagation of the main earthquake rupture. It is clear from aftershocks that the upper fault has the potential to fail seismically and we have shown that at least 0.5 mm yr^{-1} of discrete slip reaches the surface averaged over the long term. However, palaeoseismic trenching is required in order to characterize the likely slip and magnitude of earthquakes occurring on this upper segment. The Van example is also important more generally, as we have shown that in cases of sub-surface structural complexity, the effects of deeper parts of the structure on bedding-dip and topography may be masked by the larger amplitude, shorter wavelength and possibly anelastic effects arising from the shallower parts of the structure. Therefore, models of sub-surface structure built solely on surficial and upper-crustal measurements may underestimate the seismogenic depth of faulting, and might underestimate possible earthquake magnitudes or cause hazardous deep faults to remain hidden. Additionally, we have demonstrated the utility of two new techniques; SfM, a very low cost tool for accurate measurement of 3-D fault displacements, both for small creep type offsets of cm’s and fault scarps of meter displacements, and the declassified Corona mission imagery for geomorphic mapping in areas where urbanization has removed geomorphic markers. In particular SfM can be deployed very rapidly following an event in order to capture offsets due to rapidly decaying shallow afterslip and is inexpensive enough to allow frequent re-surveying.

ACKNOWLEDGEMENTS

This work was supported by funding from the UK Natural Environment Research Council (NERC) through the Looking Inside the Continents (LiCS) project (NE/K011006/1), the Earthquake without Frontiers (EwF) project (EwF_NE/J02001X/1_1) and the Centre for the Observation and Modelling of Earthquakes, Volcanoes and Tectonics (COMET, COME30001, <http://comet.nerc.ac.uk>). RTW also acknowledges support from the Royal Society. All TerraSAR-X data were provided through the GEO Supersite Initiative. Most figures were made using the public domain software Generic Mapping Tools (Wessel & Smith 1998). The authors thank two anonymous reviewers for constructive feedback and help in making this a stronger paper.

REFERENCES

- Acarel, D., Bulut, F., Bohnhoff, M. & Kartal, R., 2014. Coseismic velocity change associated with the 2011 Van earthquake (M_w 7.1): crustal response to a major event, *Geophys. Res. Lett.*, **41**(13), 4519–4526.
- Adamicc, G. & Aitken, M.J., 1998. Dose-rate conversion factor: update, *Ancient TL*, **16**(2), 37–50.
- Akinci, A. & Antonioli, A., 2013. Observations and stochastic modelling of strong ground motions for the 2011 October 23 M_w 7.1 Van, Turkey, earthquake, *Geophys. J. Int.*, **192**(3), 1217–1239.
- Allen, M.B. & Armstrong, H.A., 2008. Arabia–Eurasia collision and the forcing of mid-Cenozoic global cooling, *Palaeogeogr. Palaeoclimatol. Palaeoecol.*, **265**, 52–58.
- Altiner, Y., Söhne, W., Güney, C., Perlt, J., Wang, R. & Muzli, M., 2013. A geodetic study of the 23 October 2011 Van, Turkey earthquake, *Tectonophysics*, **588**(2013), 118–134.
- Altinli, I.E., 1966. Geology of eastern and southeastern Anatolia, *Bull. Miner. Res. Explor. Turkey*, **66**, 35–75.
- Ambraseys, N. & Melville, C., 1982. *A History of Persian Earthquakes*, Cambridge Univ. Press.
- Ambraseys, N.N., 1989. Temporary seismic quiescence: SE Turkey, *Geophys. J. Int.*, **96**(2), 311–331.
- Avouac, J.-P., Meng, L., Wei, S., Wang, T. & Ampuero, J.-P., 2015. Lower edge of locked Main Himalayan Thrust unzipped by the 2015 Gorkha earthquake, *Nat. Geosci.*, **8**(9), 708–711.
- Banerjee, D. & Murray, A., 2001. Equivalent dose estimation using a single aliquot of polymineral fine grains, *Radiat. Meas.*, **33**, 73–94.
- Bøtter-Jensen, L., 1997. Luminescence techniques: instrumentation and methods, *Radiat. Meas.*, **27**(5), 749–768.
- Bøtter-Jensen, L., Bulur, E., Duller, G.A.T. & Murray, A.S., 2000. Advances in luminescence instrument systems, *Radiat. Meas.*, **32**, 523–528.
- Brocher, T.M. et al., 2015. The M_w 6.0 24 August 2014 South Napa Earthquake, *Seismol. Res. Lett.*, **86**(2A), 309–326.
- Bronk Ramsey, C., 2009. Bayesian Analysis of Radiocarbon Dates, *Radio-carbon*, **51**(1), 337–360.
- Campbell, G.E., Walker, R.T., Abdрахmatov, K., Jackson, J., Elliott, J.R., Mackenzie, D., Middleton, T. & Schwenninger, J.-L., 2015. Great earthquakes in low strain rate continental interiors: an example from SE Kazakhstan, *J. Geophys. Res.*, **120**(8), 5507–5534.
- Copley, A. & Jackson, J., 2006. Active tectonics of the Turkish-Iranian Plateau, *Tectonics*, **25**(6), doi:10.1029/2005TC001906.
- Cukur, D., Krastel, S., Schmincke, H.-U., Sumita, M., Çağatay, M.N., Meydan, A.F., Damcı, E. & Stockhecke, M., 2014. Seismic stratigraphy of Lake Van, eastern Turkey, *Quat. Sci. Rev.*, **104**, 63–84.
- Dewey, J.F., Hempton, M.R., Kidd, W.S.F., Saroglu, F. & Sengor, A.M.C., 1986. Shortening of continental lithosphere: the neotectonics of Eastern Anatolia—a young collision zone, *Geological Society, London, Special Publications*, **19**(1), 1–36.
- Doğan, B. & Karakaş, A., 2013. Geometry of co-seismic surface ruptures and tectonic meaning of the 23 October 2011 M_w 7.1 Van earthquake (East Anatolian Region, Turkey), *J. Struct. Geol.*, **46**, 99–114.
- Doğan, U., Demir, D.Ö., Çakir, Z., Ergintav, S., Özener, H., Akoğlu, A.M., Nalbant, S.S. & Reilinger, R., 2014. Postseismic deformation following the M_w 7.2 October 23, 2011 Van earthquake (Turkey): evidence for aseismic fault reactivation, *Geophys. Res. Lett.*, **41**(7), 2334–2341.
- Dziewonski, A.M., Chou, T.-A. & Woodhouse, J.H., 1981. Determination of earthquake source parameters from waveform data for studies of global and regional seismicity, *J. geophys. Res.*, **86**(B4), 2825–2852.
- Ekström, G., Nettles, M. & Dziewoński, A., 2012. The global CMT project 2004–2010: centroid-moment tensors for 13,017 earthquakes, *Phys. Earth planet. Inter.*, **200–201**, 1–9.
- Elliott, J.R., Parsons, B., Jackson, J.A., Shan, X., Sloan, R.A. & Walker, R.T., 2011. Depth segmentation of the seismogenic continental crust: the 2008 and 2009 Qaidam earthquakes, *Geophys. Res. Lett.*, **38**(6), doi:10.1029/2011GL046897.
- Elliott, J.R., Copley, A.C., Holley, R., Scharer, K. & Parsons, B., 2013. The 2011 M_w 7.1 Van (Eastern Turkey) earthquake, *J. geophys. Res.*, **118**(4), 1619–1637.
- Elliott, J.R. et al., 2015a. The 2013 M_w 6.2 Khaki-Shonbe (Iran) Earthquake: insights into seismic and aseismic shortening of the Zagros sedimentary cover, *Earth Space Science*, **2**(11), 435–471.
- Elliott, J.R., Elliott, A.J., Hooper, A., Larsen, Y., Marinkovic, P. & Wright, T.J., 2015b. Earthquake monitoring gets boost from new satellite, *EOS, Trans. Am. geophys. Un.*, **96**(August 2014), 14–18.
- Elliott, J.R., Jolivet, R., González, P.J., Avouac, J.-P., Hollingsworth, J., Searle, M.P. & Stevens, V.L., 2016. Himalayan megathrust geometry and relation to topography revealed by the Gorkha earthquake, *Nat. Geosci.*, **9**(2), 174–180.
- Emre, Ö., Duman, T.Y., Özalp, S. & Elmacı, H., 2011. Ekim 2011 Van depremi saha gözlemleri ve kaynak faya ilişkin ön değerlendirmeler (In Turkish), Tech. rep., Mineral Research and Exploration General Directorate of Turkey, Ankara.
- Erdik, M., Kamer, Y., Demircioglu, M. & Sesetyan, K., 2012. 23 October 2011 Van (Turkey) earthquake, *Nat. Hazards*, **64**(1), 651–665.
- Evangelidis, C.P. & Kao, H., 2013. High-frequency source imaging of the 2011 October 23 Van (Eastern Turkey) earthquake by backprojection of strong motion waveforms, *Geophys. J. Int.*, **196**(2), 1060–1072.
- Fattahi, M., Walker, R.T., Khatib, M.M., Dolati, A. & Bahroudi, A., 2007. Slip-rate estimate and past earthquakes on the Doruneh fault, eastern Iran, *Geophys. J. Int.*, **168**(2), 691–709.
- Feng, W., Li, Z., Hoey, T., Zhang, Y., Wang, R., Samsonov, S., Li, Y. & Xu, Z., 2014. Patterns and mechanisms of coseismic and postseismic slips of the 2011 M_w 7.1 Van (Turkey) earthquake revealed by multi-platform synthetic aperture radar interferometry, *Tectonophysics*, **632**, 188–198.
- Fielding, E.J., Lundgren, P.R., Taymaz, T., Yolsal-Cevikbilen, S. & Owen, S.E., 2013. Fault-Slip Source Models for the 2011 M_w 7.1 Van earthquake in Turkey from SAR interferometry, pixel offset tracking, GPS, and seismic waveform analysis, *Seismol. Res. Lett.*, **84**, 579–593.
- Fonstad, M.A., Dietrich, J.T., Courville, B.C., Jensen, J.L. & Carbonneau, P.E., 2013. Topographic structure from motion: a new development in photogrammetric measurement, *Earth Surf. Process. Landf.*, **38**(4), 421–430.
- Gallovic, F., Ameri, G., Zahradnik, J., Jansky, J., Plicka, V., Sokos, E., Askan, A. & Pakzad, M., 2013. Fault process and broadband ground-motion simulations of the 23 October 2011 Van (Eastern Turkey) earthquake, *Bull. seism. Soc. Am.*, **103**(6), 3164–3178.
- Gülkan, P., Gürpınar, A., Celebi, M., Arpat, E. & Gencoğlu, S., 1978. *Engineering Report on the Muradiye-Çaldıran, Turkey, Earthquake of 24 November 1976*, National Academy of Sciences.
- Hollingsworth, J., Leprince, S., Ayoub, F. & Avouac, J.-P., 2012. Deformation during the 1975–1984 Krafla rifting crisis, NE Iceland, measured from historical optical imagery, *J. geophys. Res.*, **117**, B11407, doi:10.1029/2012JB009140.
- Hudnut, K.W. et al., 2014. Key recovery factors for the August 24, 2014, South Napa earthquake, *Tech. rep.*, U.S. Geological Survey Open-File Report.
- Irmak, T.S., Doğan, B. & Karakaş, A., 2012. Source mechanism of the 23 October, 2011, Van (Turkey) earthquake ($M_w = 7.1$) and aftershocks with its tectonic implications, *Earth Planets Space*, **64**(11), 991–1003.
- James, M.R. & Robson, S., 2012. Straightforward reconstruction of 3D surfaces and topography with a camera: accuracy and geoscience application, *J. geophys. Res.*, **117**, F03017, doi:10.1029/2011JF002289.
- James, M.R. & Robson, S., 2014. Mitigating systematic error in topographic models derived from UAV and ground-based image networks, *Earth Surf. Process. Landf.*, **39**, 1413–1420.
- Johnson, K., Nissen, E., Saripalli, S., Arrowsmith, J.R., Mcgarey, P., Williams, P. & Blisniuk, K., 2014. Rapid mapping of ultrafine fault zone topography with structure from motion, *Geosphere*, **10**(5), 969–986.
- Kadioğlu, M., Şen, Z. & Batur, E., 1997. The greatest soda-water lake in the world and how it is influenced by climatic change, *Annales Geophysicae*, **15**, 1489–1497.
- Karakhanian, A.S. et al., 2004. Active faulting and natural hazards in Armenia, eastern Turkey and northwestern Iran, *Tectonophysics*, **380**(3–4), 189–219.
- Kuzucuoğlu, C. et al., 2010. Formation of the Upper Pleistocene terraces of Lake Van (Turkey), *J. Quat. Sci.*, **25**(7), 1124–1137.

- Lienkaemper, J.J., DeLong, S.B., Domrose, C.J. & Rosa, C.M., 2016. Afterslip behavior following the 2014 M 6.0 South Napa Earthquake with implications for Afterslip forecasting on other seismogenic faults, *Seismol. Res. Lett.*, **87**(3), 609–619.
- Litt, T. & Anselmetti, F.S., 2014. Lake Van deep drilling project PALEOVAN, *Quat. Sci. Rev.*, **104**, 1–7.
- Litt, T. *et al.*, 2009. 'PALEOVAN', International Continental Scientific Drilling Program (ICDP): site survey results and perspectives, *Quat. Sci. Rev.*, **28**(15–16), 1555–1567.
- Litt, T. *et al.*, 2012. Scientific Drilling, *Sci. Drill.*, **14**, 18–29.
- Lowe, D.G., 2004. Distinctive Image Features from Scale-Invariant Keypoints, *Int. J. Comput. Vis.*, **60**(2), 91–110.
- McClusky, S. *et al.*, 2000. Global Positioning System constraints on plate kinematics and dynamics in the eastern Mediterranean and Caucasus, *J. geophys. Res.*, **105**(B3), 5695–5719.
- Mejdahl, V., 1979. Thermoluminescence dating: beta-dose attenuation in quartz grains, *Archaeometry*, **21**(1), 61–72.
- Moro, M. *et al.*, 2014. The October 23, 2011, Van (Turkey) earthquake and its relationship with neighbouring structures, *Sci. Rep.*, **4**, 3959, doi:10.1038/srep03959.
- MTA, 2002. *1:500 000 Scale Geological Maps of Turkey*, Van Section, Mineral Research & Exploration General Directorate Press, Ankara.
- Murray, A. & Wintle, A., 2000. Luminescence dating of quartz using an improved single-aliquot regenerative-dose protocol, *Radiat. Meas.*, **32**(1), 57–73.
- Nissen, E., Yamini-Fard, F., Tatar, M., Gholamzadeh, A., Bergman, E., Elliott, J.R., Jackson, J.A. & Parsons, B., 2010. The vertical separation of mainshock rupture and microseismicity at Qeshm island in the Zagros fold-and-thrust belt, Iran, *Earth planet. Sci. Lett.*, **296**(3–4), 181–194.
- Okada, Y., 1985. Surface deformation due to shear and tensile faults in a half-space, *Bull. seism. Soc. Am.*, **75**(4), 1135–1154.
- Özkaymak, Ç., Sağlam, A. & Köse, O., 2003. Active tectonic characteristics of the east of Lake Van (East Anatolian, Turkey), in *ATAG-7 Active Tectonics Research Group 7th Symposium*, pp. 54–60.
- Özkaymak, C., Sozobilir, H., Bozkurt, E., Dirik, K., Topal, T., Alan, H. & Caglan, D., 2011. Seismic geomorphology of October 23, 2011 Tabanlı-Van earthquake and its relation to active tectonics of East Anatolia (in Turkish), *J. Geol. Eng.*, **35**(2), 175–199.
- Pearce, J.A. *et al.*, 1990. Genesis of collision volcanism in Eastern Anatolia, Turkey, *J. Volcanol. Geotherm. Res.*, **44**(1–2), 189–229.
- Prescott, J. & Hutton, J., 1994. Cosmic ray contributions to dose rates for luminescence and ESR dating: large depths and long-term time variations, *Radiat. Meas.*, **23**(1), 497–500.
- Reilinger, R. *et al.*, 2006. GPS constraints on continental deformation in the Africa–Arabia–Eurasia continental collision zone and implications for the dynamics of plate interactions, *J. geophys. Res.*, **111**, B05411, doi:10.1029/2005JB004051.
- Reimer, P., 2013. IntCal13 and Marine13 radiocarbon age calibration curves 0–50,000 years cal BP, *Radiocarbon*, **55**(4), 1869–1887.
- Rhodes, E.J., 2015. Dating sediments using potassium feldspar single-grain IRSL: initial methodological considerations, *Quat. Int.*, **362**, 14–22.
- Rosen, P.A., Hensley, S., Peltzer, G. & Simons, M., 2004. Updated repeat orbit interferometry package released, *EOS, Trans. Am. geophys. Un.*, **85**(5), 47, doi:10.1029/2004EO050004.
- Saroglu, F., Emre, Ö. & Kuşçu, I., 1992. Active Fault Map of Turkey, Tech. rep., General Directorate of Mineral Research and Exploration (MTA), Eskisehir Yolu, 06520, Ankara, Turkey.
- Shebalin, N. *et al.*, 1997. Caucasus test-area strong earthquake catalogue, in *Historical and Prehistorical Earthquakes in the Caucasus*, pp. 210–223, eds Giardini, D. & Balassanian, S., Kluwer Academic Publishing.
- Smith, W. & Wessel, P., 1990. Gridding with continuous curvature splines in tension, *Geophysics*, **55**(3), 293–305.
- Stockhecke, M. *et al.*, 2014. Sedimentary evolution and environmental history of Lake Van (Turkey) over the past 600 000 years, *Sedimentology*, **61**(6), 1830–1861.
- Thierry, J.M., 1979. Monasteres Armeniens du Vaspurakan, *Rev. Etud. Armeniens*, **9**, 137–178.
- Üner, S., Yeşilova, Ç. & Yakupoğlu, T., 2012. *The Traces of Earthquake (Seismites): Examples from Lake Van Deposits (Turkey)*, InTech.
- Üner, S., Okuldaş, C. & Yılmaz, A.V., 2015. Structural and sedimentological properties of Lacustrine deposits in Pliocene Dorutay Basin (Özalp-Van) (In Turkish), *Bull. Earth Sci. Appl. Res. Cent. Hacettepe Univ.*, **36**(1), 19–30.
- Utucu, M., 2013. 23 October 2011 Van, Eastern Anatolia, earthquake (MW 7.1) and seismotectonics of Lake Van area, *J. Seismol.*, **17**(2), 783–805.
- Vernant, P. *et al.*, 2004. Present-day crustal deformation and plate kinematics in the Middle East constrained by GPS measurements in Iran and northern Oman, *Geophys. J. Int.*, **157**, 381–398.
- Walker, R.T. & Fattahi, M., 2011. A framework of Holocene and Late Pleistocene environmental change in eastern Iran inferred from the dating of periods of alluvial fan abandonment, river terracing, and lake deposition, *Quat. Sci. Rev.*, **30**(9–10), 1256–1271.
- Wang, C., Ding, X., Li, Q., Shan, X., Zhu, W., Guo, B. & Liu, P., 2015. Co-seismic and postseismic slip models of the 2011 Van earthquake, Turkey, from InSAR, offset-tracking, MAI, and GPS observations, *J. Geodyn.*, **91**, 39–50.
- Wells, D.L. & Coppersmith, K.J., 1994. New empirical relationships among magnitude, rupture length, rupture width, rupture area, and surface displacement, *Bull. seism. Soc. Am.*, **84**(4), 974–1002.
- Wesnousky, S.G., 2008. Displacement and geometrical characteristics of earthquake surface ruptures: issues and implications for seismic-hazard analysis and the process of earthquake rupture, *Bull. seism. Soc. Am.*, **98**(4), 1609–1632.
- Wessel, P. & Smith, W.H.F., 1998. New, improved version of generic mapping tools released, *EOS, Trans. Am. geophys. Un.*, **79**(47), 579–579.
- Wintle, A.G. & Murray, A.S., 2006. A review of quartz optically stimulated luminescence characteristics and their relevance in single-aliquot regeneration dating protocols, *Radiat. Meas.*, **41**(4), 369–391.
- Wright, T.J., Elliott, J.R., Wang, H. & Ryder, I., 2013. Earthquake cycle deformation and the Moho: implications for the rheology of continental lithosphere, *Tectonophysics*, **609**, 504–523.
- Zahradnik, J. & Sokos, E., 2011. *Multiple-point source solution of the Mw7.2 Van earthquake, October 23, 2011, Eastern Turkey*, Tech. rep., European-Mediterranean Seismological Centre (EMSC).
- Zahradnik, J. & Sokos, E., 2014. The Mw 7.1 Van, Eastern Turkey, earthquake 2011: two-point source modelling by iterative deconvolution and non-negative least squares, *Geophys. J. Int.*, **196**(1), 522–538.
- Zimmerman, D.W., 1971. Thermoluminescence dating using fine grains from pottery, *Archaeometry*, **13**(1), 29–52.

APPENDIX A: OPTICALLY STIMULATED LUMINESCENCE DATING

OSL dating was performed on quartz grains from sediment samples collected in well packed stainless steel tubes to ensure sample stability in transport. Sample preparation was carried out under low-intensity light emitting diode (LED) light (at ~588 nm), to yield clean, sand-sized (180–250 µm) quartz, using standard methods including wet-sieving, HCL acid digestion, heavy liquid separation and etching in concentrated HF (40 per cent) to dissolve potassium feldspar minerals and the alpha-dosed outer layer of the quartz grains. At least 12 aliquots were prepared and measured for each sample, mounting the quartz grains as a multigrain monolayer on aluminium disks of ~4 mm diameter using a silicon oil adhesive. To estimate the burial age of our samples, we need two components, the equivalent dose *De* (integrated radiation required to produce the luminescence signal observed) and the environmental dose rate received during burial.

The equivalent dose (*De*) was recovered using the single aliquot regeneration measurement protocol (Murray & Wintle 2000; Wintle & Murray 2006), conducted on an automated TL/DA-15 Risø luminescence reader (Bøtter-Jensen 1997; Bøtter-Jensen *et al.* 2000).

The sample was bleached with clusters of 870 nm infrared LEDs providing circa 131 mW cm^{-2} at 50°C for 100 s to confirm the absence of any infrared sensitive signal (Banerjee & Murray 2001), before blue light stimulation with clusters of blue LEDs (42 Nichia $470\Delta 20 \text{ nm}$, $\sim 34 \text{ W cm}^{-2}$) at a raised temperature of 125° . The natural and regenerative luminescence dose samples were preheated at 260°C for 10 s, while the fixed test dose samples (to calibrate for sensitivity change) were preheated to 240°C for 10 s prior to optical stimulation. Ultraviolet ($\sim 370 \text{ nm}$) OSL emission was measured using an Electron Tubes Ltd 9235QA photomultiplier tube fitted with a blue-green sensitive bialkali photocathode and either two Corning U-340 glass filters or a 7.5 mm Hoya U-340 glass filter.

After measuring the natural luminescence, a calibrated $^{90}\text{Sr}/^{90}\text{Y}$ beta source housed in the reader was used to construct the regenerative dose response curve. The luminescences were measured at 6–8 different doses, including a zero dose point and a duplicate measurement of the lowest regenerative dose to check recovery. Following each luminescence measurement, a test dose and second

pre-heat are applied to the aliquot to normalize the luminescence measurement and calibrate for sensitivity change (Murray & Wintle 2000). Fitting a dose response curve, we determined the equivalent dose D_e from the natural luminescence.

The 5 cm of sediment at either end of the collection tube (deemed to have been exposed to light), was used to estimate the concentrations of potassium-40, uranium-238 and thorium-232 by inductively coupled plasma mass spectrometry (ICP-MS) with a lithium metaborate/tetraborate fusion. These concentrations are used to estimate an environmental dose rate from the gamma and beta components of the decay chains for ^{40}K , ^{232}Th , ^{238}U , using the attenuation factors estimated by Adamiec & Aitken (1998), with corrections for water content (Zimmerman 1971) and grain size Mejdahl (1979). We estimate a cosmic ray dose rate based on data reported by Prescott & Hutton (1994), accounting for the geomagnetic latitude and elevation along with the density and thickness of the overburden. Table 3 shows the OSL ages determined, with the relevant site and the displacement at that site.